Dynamic Simulation-Guided Design of Tumbling Magnetic Microrobots

Jiayin Xie
Department of Mechanical Engineering,
Stony Brook University,
Stony Brook, NY 11794
e-mail: jiayin.xie@stonybrook.edu

Chenghao Bi
School of Mechanical Engineering,
Purdue University,
West Lafayette, IN 47907
e-mail: bi10@purdue.edu

David J. Cappelleri
School of Mechanical Engineering,
Purdue University,
West Lafayette, IN 47907
e-mail: dcappell@purdue.edu

Nilanjan Chakraborty[1]
Department of Mechanical Engineering,
Stony Brook University,
Stony Brook, NY 11794
e-mail: nilanjan.chakraborty@stonybrook.edu

The design of robots at the small scale is a trial-and-error based process, which is costly and time-consuming. There are few dynamic simulation tools available to accurately predict the motion or performance of untethered microrobots as they move over a substrate. At smaller length scales, the influence of adhesion and friction, which scales with surface area, becomes more pronounced. Thus, rigid body dynamic simulators, which implicitly assume that contact between two bodies can be modeled as point contact, are not suitable. In this paper, we present techniques for simulating the motion of microrobots where there can be intermittent and non-point contact between the robot and the substrate. We use these techniques to study the motion of tumbling microrobots of different shapes and select shapes that are optimal for improving locomotion performance. Simulation results are verified using experimental data on linear velocity, maximum climbable incline angle, and microrobot trajectory. Microrobots with improved geometry were fabricated, but limitations in the fabrication process resulted in unexpected manufacturing errors and material/size scale adjustments. The developed simulation model can incorporate these limitations and emulate their effect on the microrobot's motion, reproducing the experimental behavior of the tumbling microrobots, further showcasing the effectiveness of having such a dynamic model. [DOI: 10.1115/1.4050098]

Keywords: dynamics, microscale mechanisms and robotics

1 Introduction

Tumbling microrobots have the potential to go to previously unreachable areas of the body and perform tasks such as targeted drug delivery, tissue biopsies, and toxin neutralization [1]. Magnetically actuated tumbling microrobots use the difference in the orientation between the robot's internal magnetization and that of a rotating external magnetic field to induce magnetic torque on the robot, making it tumble forward end-over-end, and several designs have been proposed in the literature [2–11].

Rolling locomotion using a rotating permanent magnet was demonstrated using a spherical magnetic microrobot [2]. The microrobot consisted of a 440 μm diameter UV adhesive ball encapsulating a 30 μm diameter iron wire. It was shown to be capable of moving in air, water, and silicone oil over flat and bumpy surfaces. A transversely magnetized rolling magnetic microrobot was developed, and locomotion and non-contact micromanipulation in a fluidic environment was demonstrated in Refs. [6,7]. The microrobot design consists of a $50 \times 60 \times 300$ μm polymeric block with internal cobalt–nickel posts that roll continuously about its long axis to generate a fluid vortex above it while simultaneously translating forward. Tumbling locomotion using rotating magnetic fields exhibits similar performance over arbitrary surfaces in dry air conditions. A rectangular stainless steel microrobot tumbling over an acrylic plate and over the surface of a coin was achieved in Ref. [3]. Similarly, tumbling locomotion has been shown to be versatile in both wet and dry environments, on steep inclines, and on rough surfaces [8] and more recently in both in vitro [9] and in vivo [11] biomedical environments. Figure 1 shows the schematic sketch of such a tumbling microrobot. The external magnetic fields actuating the robot harmlessly penetrate living tissue and allow for tetherless locomotion. One key limitation of external magnetic fields, however, is that they decrease roughly volumetrically in strength as distance increases between the magnetic target and the source of the field. Therefore, it is beneficial to optimize the robot's design to achieve the most mobility under limited magnetic field strengths. It is also beneficial to optimize the design to travel over as many different surfaces as possible.

Currently, the design of tumbling microrobots is a trial-and-error based process, which is costly and time-consuming. Thus, a flexible dynamic simulation tool for virtual design iteration and optimization would be highly valuable. Therefore, *our goal in this paper is to create a dynamic simulation tool that can be used to study the motion of microrobots of different geometry and manufacture a subset of the robots for experimentation*. This complements the existing efforts in microrobot design, which are based on the designers' intuition, and will greatly help reduce the cost and effort of the microrobot design process, as the designer can hone in on the most promising designs. The development and use of

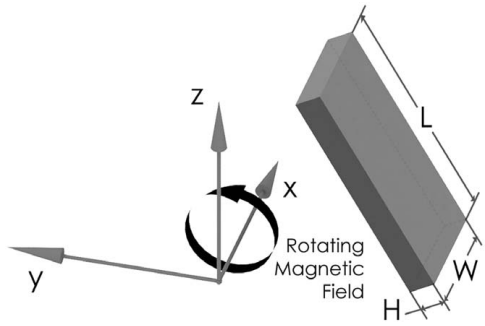

Fig. 1 Microscale magnetic tumbling (μTUM) robot tumbles on a planar surface. A magnetic field rotating counterclockwise about the *x*-axis causes the robot to rotate about the same direction and tumble forward (along the direction of *y*-axis). The length, width, and height of the μTUM robot are L, W, and H, respectively.

[1]Corresponding author.

Contributed by the Mechanisms and Robotics Committee of ASME for publication in the Journal of Mechanisms and Robotics. Manuscript received June 22, 2020; final manuscript received January 25, 2021; published online April 9, 2021. Assoc. Editor: Jonathan Hopkins.

the dynamic simulation tool in the iterative design process of tumbling microrobots is a key novelty of the paper.

A critical challenge for simulating the tumbling microrobot is to model the intermittent and non-point contact between the robot and substrate, which will change during the motion based on the contact mode. For example, for the box-like microrobot (shown in Fig. 1), tumbling over a flat surface will alternate between area contact and line contact as it flips end over end. Furthermore, the contact area will change depending on the face that is in contact. This is crucial because, at the length scale of microrobots, the dynamics are heavily influenced by adhesive forces that scale with the surface area.

Most existing dynamic simulation methods for microrobots [12,13] implicitly assume that the contact between two bodies can be modeled as point contact. They choose contact points a priori in an ad hoc manner to represent the contact patch. For the tumbling robot, since the contact patch is time-varying, it is not possible to choose a contact point a priori and would thus introduce inaccuracy in simulation. Recently, we developed principled methods [14–16] to simulate intermittently contacting rigid bodies with planar convex and non-convex contact patches. In this paper, based on our previous work, we develop a method for simulating the motion of microrobots where the contact between the robot and the substrate is intermittent and possibly non-point.

Contributions: The key contributions of this paper are as follows: (a) This paper presents a novel discrete-time dynamic model and simulation approach for predicting the motion of microrobots that (i) can automatically handle switches between different contact modes like point, line, and surface contact, as well as sticking and slipping at the contact and (ii) can incorporate surface area-dependent adhesive forces that change with the different contact modes. (b) The use of the dynamic simulation tool for design domain exploration to select a subset of promising tumbling microrobot geometries is demonstrated. Geometric shapes that best improve locomotion performance in terms of linear velocity and maximum climbable incline angle are identified through simulation. (c) The motion prediction model is also used to study the sensitivity of the motion of the designed microrobots to manufacturing errors. (d) Experimental studies are performed to validate the simulations. The best microrobots identified from the design space exploration are manufactured, and their motion behavior is experimentally characterized. The resulting motion behaviors show a good match with the simulations.

A preliminary version of this paper appeared in Ref. [17]. In this paper, we have rewritten some sections of Ref. [17] for clarity. Furthermore, we have added an extensive simulation analysis of the design space and reported additional experimental studies supporting the simulation studies.

Outline of the Paper: This paper starts by discussing related work on dynamic models in Sec. 2, with additional comments on microscale effects. Section 3 then provides a high-level overview of the design space explored in this work. In Sec. 4, our general dynamic model is described in detail and further refined for tumbling microrobots in Sec. 5. Next, in Sec. 6, we verify the results of the dynamic model with a variety of experimental locomotion tests. Performance predictions are made in Sec. 7 for four alternative tumbling microrobot geometries, and Sec. 8 describes the manufacturing process and limitations for fabricating the two best performing designs. Sec. 9 discusses the incorporation of manufacturing errors into the dynamic model and compares the altered motion prediction results with experimental data from the two alternative microrobot designs. Conclusions about tumbling microrobot performance and the capabilities of the dynamic model are discussed in Sec. 10. Finally, concluding thoughts and a future outlook are described in Sec. 11.

2 Related Work

Past literature has demonstrated dynamic models for several mobile microrobots. Pawashe et al. simulated a planar microrobot with stick-slip motion over dry horizontal surfaces [12,13]. The simulation was able to predict the robot's orientation and linear velocity over time under various external field parameters and surface properties. However, this model does not consider tumbling locomotion with non-point contact patches. Hu et al. developed models for predicting the velocities of the rolling, walking, and crawling gaits of a soft-bodied magnetic millibot capable of multimodal locomotion [18]. The model helped determined which geometric dimensions were critical for the success of particular gaits of the robot. Morozov et al. proposed a general theory to study the dynamics of arbitrarily shaped magnetic propellers and rationalize previously unexplained experimental observations [19]. To date, a comprehensive three-dimensional model that can predict a microrobot's trajectory and velocity over time with consideration of intermittent contact, non-point contact, and inclined or unstructured surfaces has yet to be developed.

In this paper, we present techniques for simulating motion of microrobots where there can be intermittent and non-point contact between the robot and the surface. The model we use is called a differential complementarity problem (DCP). Let $\mathbf{u} \in \mathbb{R}^{n_1}$, $\mathbf{v} \in \mathbb{R}^{n_2}$ and let $\mathbf{g}:\mathbb{R}^{n_1} \times \mathbb{R}^{n_2} \to \mathbb{R}^{n_1}$, $\mathbf{f}:\mathbb{R}^{n_1} \times \mathbb{R}^{n_2} \to \mathbb{R}^{n_2}$ be two vector functions, and the notation $0 \le \mathbf{x} \perp \mathbf{y} \ge 0$ implies that $\mathbf{x}$ is orthogonal to $\mathbf{y}$, and each component of the vectors is non-negative.

DEFINITION 1. *The differential (or dynamic) complementarity problem is to find* $\mathbf{u}$ *and* $\mathbf{v}$ *satisfying [20]*

$$\dot{\mathbf{u}} = \mathbf{g}(\mathbf{u}, \mathbf{v}), \quad 0 \le \mathbf{v} \perp \mathbf{f}(\mathbf{u}, \mathbf{v}) \ge 0$$

DEFINITION 2. *The mixed complementarity problem is to find u and v satisfying*

$$\mathbf{g}(\mathbf{u}, \mathbf{v}) = 0, \quad 0 \le \mathbf{v} \perp \mathbf{f}(\mathbf{u}, \mathbf{v}) \ge 0$$

If the functions $\mathbf{f}$ and $\mathbf{g}$ are linear, the problem is called a mixed linear complementarity problem (MLCP). Otherwise, the problem is called a mixed nonlinear complementarity problem (MNCP). As we will discuss later, our discrete-time dynamics model is an MNCP.

Modeling the intermittent contact between bodies in motion as a complementarity constraint was first done by Lotstedt [21]. Subsequently, there was a substantial amount of effort in modeling and dynamic simulation with complementarity constraints [22–29]. The DCP that models the equations of motion usually can not be solved in closed form. Therefore, a time-stepping scheme has been introduced to solve the DCP. Depending on the assumptions made when forming the discrete equation of motions, the discrete-time model can be divided into an MLCP problem [30,31] and an MNCP problem [32,33]. Furthermore, depending on whether the distance function between the two bodies (which is a nonlinear function of the configuration) is approximated or linearized, the time-stepping scheme can also be further divided into geometrically explicit schemes [23,25] and geometrically implicit schemes [14,32,33].

All of the time-stepping schemes mentioned above assume the contact between two objects to be point contact. However, at the microscale, the influence of adhesion and friction becomes more pronounced. Both of these factors scale with the surface contact area. Recently, we presented a dynamic model that takes non-point contact (where the contact mode could be point contact, line contact, or surface contact) into account [14]. The model belongs to a geometrically implicit time-stepping scheme, in which the distance function depends on the geometry and configurations of the rigid body. In this paper, we extend this model to handle surface area-dependent adhesive forces of a rigid body microrobot that will change during motion based on the contact mode. The resulting discrete-time model is an MNCP problem.

There has been much effort to model and understand the effect of non-point frictional contact [34–36]. We use the so called soft-finger contact model [37] for the general dynamic simulation.

The model is based on a maximum power dissipation principle, and it assumes all the possible contact forces or moments should lie within an ellipsoid. At the microscale, adhesion is more pronounced and can have a significant effect on microrobot locomotion. It is the combined effect of forces that may stem from capillary effects, electrostatic charging, covalent bonding, hydrogen bonding, Casimir forces, or Van der Waals interactions [38]. All of these forces, aside from forces arising from electrostatic charging, become negligible outside of the nanometer range. Van der Waals forces, for example, primarily act at ranges of 0.2–20 nm [39]. These forces can also be unpredictable and difficult to model individually. Therefore, we lumped the forces together into a single adhesion force and assume its effect is insignificant if there is no direct contact between the microrobot and the substrate. We formulated this adhesive force as an empirical relationship where it is proportional to the surface contact area. This relationship is useful because our dynamic model is capable of predicting the time-varying surface contact area. The electrostatic force is treated as a constant since the distance between the microrobot and the substrate undergoes minimal change as the robot moves.

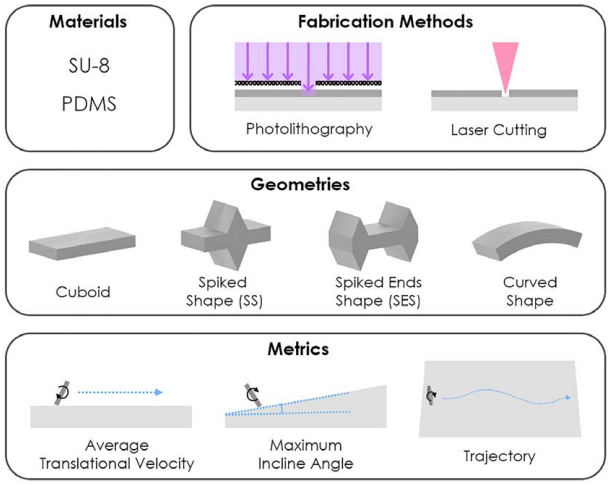

Fig. 2 Overview of the tumbling microrobot design domain showing the materials, fabrication methods, and the geometries that we considered, as well as the metrics used to evaluate them

3 Design Domain

There is an increasingly vast set of materials and fabrication methods available for manufacturing complex structures at the microscale. In this paper, we investigate a small subset of these options that show potential for the purposes of tumbling magnetic microrobots. We consider two materials, SU-8 and PDMS (polydimethylsiloxane), which are both polymers frequently used in microfluidics and MEMS applications. SU-8 is a negative photoresist that is sensitive to UV light and can form very rigid, high aspect ratio structures after becoming cross-linked [40]. It shows exceptional biocompatibility and has been used for several biomedical applications such as cell encapsulation and neuronal probes [41]. Similarly, PDMS is a biocompatible silicone-based elastomer that cross-links to form solids with rubber-like consistency. It is the most commonly used material in the domain of experimental microfluidics, among other applications, due to its cost-effectiveness, excellent biocompatibility and permeability, low autofluorescence, and transparency [42]. Both SU-8 and PDMS are still capable of cross-linking into solid structures after being doped with magnetic neodymium iron boron (NdFeB) particles, allowing tumbling microrobots to be formed from either material. Although difficult to machine using traditional manufacturing methods, thin films of SU-8 and PDMS can be processed into complex geometries with nanoscale resolution using photolithography or laser cutting processes. Both these fabrication methods, however, are limited to producing flat, two-dimensional geometries and experience reduced performance when incorporating doped magnetic particles.

The limitations set by these fabrication methods drive the shape space that is explored. In addition to the basic cuboid shape characterized in Ref. [8], we consider alternative geometries for the tumbling microrobot, including a spiked shape (SS), a spiked ends shape (SES), and a curved shape. These new designs feature altered cross sections and seek to improve microrobot responsiveness by minimizing area contact during the tumbling cycle and decreasing resistive adhesive forces. Our objective for the dynamic model is to use it for studying and predicting the best performing design without expending resources on iterative prototyping of physical microrobots. We also use it for understanding the robustness of the design to manufacturing errors. Metrics for evaluating degrees of microrobot performance include the average translational velocity in the desired direction of motion, maximum climbable incline angle, and positional trajectory during the tumbling cycle. This data can all be captured optically using a digital microscope and furthered quantified using image processing. A high-level overview of this paper's design domain is depicted in Fig. 2.

4 Dynamic Model for Rigid Body Systems

In this section, we present an overview of the equations of motion of two rigid bodies in intermittent contact with each other. A microrobot moving on a surface may switch between having contact with the surface or no contact at all. Furthermore, when the robot is in contact, the contact may be a sliding or sticking contact (i.e., no relative velocity between the points on the objects in the contact region). Depending on the geometry of the robot and its configuration, the contact mode may also be point contact, line contact, or surface contact. A key requirement for building dynamic simulators for the microrobots is the ability to handle surface area-dependent adhesive forces that will change during motion based on the contact mode. We will therefore use a complementarity-based model of dynamics that can handle the transition between no-contact and contact as well as sticking and sliding contact in a unified manner. Furthermore, since we can have non-point contact, we will use the equations of motion in Ref. [14] as our basic model for the dynamics.

When fabricating the microrobots, manufacturing errors inevitably exist. It is possible that these errors in geometry and/or magnetization axis alignment may cause the microrobots to tilt or flip unexpectedly during the tumbling motion. Thus, the motion of the microrobot is not restricted to a two-dimensional plane and the three-dimensional dynamic model in Ref. [14] is necessary to simulate the dynamics of the microrobots.

The general equations of motion have three key parts: (i) Newton–Euler differential equations of motion giving state updates, (ii) algebraic and complementarity constraints modeling the fact that two rigid bodies cannot penetrate each other, and (iii) a model of the contact force and moments acting on the contact patch. For general rigid body motion, the model of contact forces and moments use Coulomb's assumption that *the normal force acting between two objects is independent of the nominal contact area between the two objects*. This is a reasonable assumption for nominally rigid objects at macroscopic length scales, where the inertial forces are dominating. However, at the length-scale of microrobots, the force of adhesion between the contacting surfaces is comparable to inertial forces. So, the contact model should also take into consideration the effect of the surface-area dependent forces. These forces, combined under a single adhesive force, are illustrated in Fig. 3.

For simplicity of exposition, we assume one body to be static. Let $\mathbf{V} = [\mathbf{v}^T \boldsymbol{\omega}^T]^T$ be the generalized velocity of the rigid body, where $\mathbf{v} \in \mathbb{R}^3$ is the linear velocity and $\boldsymbol{\omega} \in \mathbb{R}^3$ is the angular velocity of the rigid body. Let $\mathbf{q}$ be the position of the center of mass (CM) of

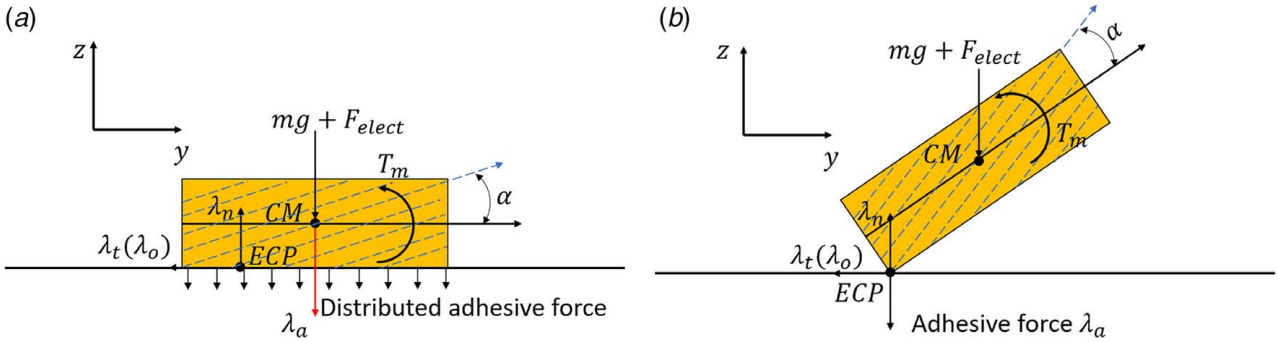

Fig. 3 Force diagrams in 2D when robot has (*a*) surface contact and (*b*) line contact with horizontal surface in 2D. The dashed lines represent the internal magnetic alignment, and its arrow represents the magnetic alignment's direction. The adhesive force is distributed uniformly over the surface area. When robot has line contact with the surface, the adhesive force is almost zero.

the object, and the orientation of the object in an inertial frame ($\mathbf{q}$ can be a 6×1 or 7×1 vector depending on the representation of the orientation). We will use unit quaternions to represent the orientation unless otherwise stated.

Newton–Euler Equations of Motion: The Newton–Euler equations of motion of the rigid body is

$$\mathbf{M}(\mathbf{q})\dot{V} = \mathbf{W}_n\lambda_n + \mathbf{W}_t\lambda_t + \mathbf{W}_o\lambda_o + \mathbf{W}_r\lambda_r + \boldsymbol{\lambda}_{app} + \boldsymbol{\lambda}_{vp} \tag{1}$$

where the matrix $\mathbf{M}(\mathbf{q}) \in \mathbb{R}^{6\times6}$ is the inertia tensor, the vector $\boldsymbol{\lambda}_{app} \in \mathbb{R}^6$ is the external forces and moments (including gravity), and the vector $\boldsymbol{\lambda}_{vp} \in \mathbb{R}^6$ is the centripetal and Coriolis forces. The magnitude of the normal contact force is λ_n. The magnitude of tangential contact forces is λ_t and λ_o. The magnitude of the moment due to the tangential contact forces about the contact normal is λ_r. The vectors $\mathbf{W}_n, \mathbf{W}_t, \mathbf{W}_o, \mathbf{W}_r \in \mathbb{R}^6$ map the contact forces and moments from the contact point to the center of mass of the robot. The expressions of $\mathbf{W}_n$, $\mathbf{W}_t$, $\mathbf{W}_o$, and $\mathbf{W}_r$ are

$$\mathbf{W}_n = \begin{bmatrix} \mathbf{n} \\ \mathbf{r}\times\mathbf{n} \end{bmatrix}, \mathbf{W}_t = \begin{bmatrix} \mathbf{t} \\ \mathbf{r}\times\mathbf{t} \end{bmatrix}, \mathbf{W}_o = \begin{bmatrix} \mathbf{o} \\ \mathbf{r}\times\mathbf{o} \end{bmatrix}, \mathbf{W}_r = \begin{bmatrix} \mathbf{0} \\ \boldsymbol{n} \end{bmatrix} \tag{2}$$

where $(\mathbf{n}, \mathbf{t}, \mathbf{o}) \in \mathbb{R}^3$ are the axes of the contact frame, and $\mathbf{0} \in \mathbb{R}^3$ is a column vector with each entry equal to zero. As shown in Fig. 3, vector $\mathbf{r} = [a_x - q_x,\ a_y - q_y,\ a_z - q_z]$ is the vector from equivalent contact point (ECP) $\mathbf{a} \in \mathbb{R}^3$, to CM, where (q_x, q_y, q_z) is the position of the CM. In the next section, we will provide a definition for the ECP. Please note that Eq. (1) is a system of six differential equations.

Modeling Rigid Body Contact Constraints: The contact model that we use is a complementarity-based contact model as described in Refs. [14,33]. In Ref. [14], we introduced the notion of an ECP to model non-point contact between objects.

DEFINITION 3. *ECP is a unique point on the contact surface that can be used to model the surface (or line) contact as point contact where the integral of the total moment (about the point) due to the distributed normal force on the contact patch is zero.*

The ECP defined here is the same as the center of friction. Now let us describe the contact model mathematically. Objects F and G are defined by the intersection of convex inequalities $f_i(\boldsymbol{\zeta}_1) \le 0$, $i = 1, .., \tilde{m}$ and $g_j(\boldsymbol{\zeta}_2) \le 0$, $j = \tilde{m}+1, \ldots, \tilde{n}$, respectively. Let $\mathbf{a}_1, \mathbf{a}_2 \in \mathbb{R}^3$ be a pair of ECPs or closest points (when objects are separate) on F and G, respectively. The complementarity conditions for nonpenetration can be written as either one of the following two sets of conditions [33]:

$$\begin{aligned} 0 \le \lambda_n \perp \max_{1,\ldots,\tilde{m}} f_i(\mathbf{a}_2) \ge 0 \\ 0 \le \lambda_n \perp \max_{j=\tilde{m}+1,\ldots,\tilde{n}} g_j(\mathbf{a}_1) \ge 0 \end{aligned} \tag{3}$$

The solution of ECP's $\mathbf{a}_1$ and $\mathbf{a}_2$ is given by the following minimization problem:

$$(\mathbf{a}_1, \mathbf{a}_2) = \arg\min_{\zeta_1,\zeta_2} \{\|\boldsymbol{\zeta}_1 - \boldsymbol{\zeta}_2\| \ f_i(\boldsymbol{\zeta}_1) \le 0,\ \ g_j(\boldsymbol{\zeta}_2) \le 0\} \tag{4}$$

where $i = 1, \ldots, \tilde{m}$ and $j = \tilde{m}+1, \ldots, \tilde{n}$.

Using a slight modification of the Karush–Kuhn–Tucker (KKT) conditions for the optimization problem in Eq. (4), and combining it with either one of the conditions in Eq. (3), we get the complete contact model between two rigid bodies:

$$\begin{aligned} &\mathbf{a}_1 - \mathbf{a}_2 = -l_k\mathcal{C}(\mathbf{F}, \mathbf{a}_1),\ \ \mathcal{C}(\mathbf{F}, \mathbf{a}_1) = -\mathcal{C}(\mathbf{G}, \mathbf{a}_2) \\ &0 \le \begin{bmatrix} \mathbf{l}_1 \\ \mathbf{l}_2 \\ \lambda_n \end{bmatrix} \perp \begin{bmatrix} -\mathbf{f}(\mathbf{a}_1), \\ -\mathbf{g}(\mathbf{a}_2), \\ \max_j \mathbf{f}(\mathbf{a}_2) \end{bmatrix} \ge 0 \\ &i = 1, \ldots, \tilde{m},\quad j = \tilde{m}+1, \ldots, \tilde{n} \end{aligned} \tag{5}$$

where k is the index of active constraint on body F, and the normal cones are $\mathcal{C}(\mathbf{F}, \mathbf{a}_1) = \nabla f_k(\mathbf{a}_1) + \sum_{i=1, i\ne k}^{\tilde{m}} l_i \nabla f_i(\mathbf{a}_1)$, $\mathcal{C}(\mathbf{G}, \mathbf{a}_2) = \sum_{j=\tilde{m}+1}^{\tilde{n}} l_j \nabla g_j(\mathbf{a}_2)$. The vectors $\mathbf{l}_1 = [l_1, \ldots, l_{\tilde{m}}]$, $\mathbf{l}_2 = [l_{\tilde{m}+1}, \ldots, l_{\tilde{n}}]$ concatenate the Lagrange multipliers in contact constraints.

Friction Model: We use a friction model based on the maximum power dissipation principle, which has been previously proposed in the literature for point contact [22]. The maximum power dissipation principle states that among all the possible contact forces and moments that lie within the friction ellipsoid, the forces that maximize the power dissipation at the contact point are selected. For non-point contact, we will use a generalization of the maximum power dissipation principle, where we select contact forces/moments and contact velocities that maximize the power dissipation over the entire contact patch. We will now show that the problem formulation using the power loss over the whole contact patch can be reduced to the friction model for point contact with the ECP as the chosen point. Mathematically, the power dissipated over the entire surface, P_c, is

$$P_c = -\int_A (v_{ti}\beta_{ti} + v_{oi}\beta_{oi} + v_{ri}\beta_{ri})dA \tag{6}$$

where v_{ti}, v_{oi} are the linear sliding velocities and v_{ri} is the angular velocity at dA, β_{ti}, β_{oi} are the frictional force per unit area and β_{ri} is the resistive moment per unit area at dA, about the normal to the contact patch. We will assume a planar contact patch which implies that the contact normal is the same at all points on the contact patch. As shown in Fig. 4, the angular velocity is constant across the contact patch, i.e., $v_{ri} = v_r$, for all i. Let v_t and v_o be the components of tangential velocities at the ECP. From basic kinematics, we know that $v_{ti} = v_t - v_{ri}(a_{yi} - a_y)$ and $v_{oi} = v_o + v_{ri}(a_{xi} -$

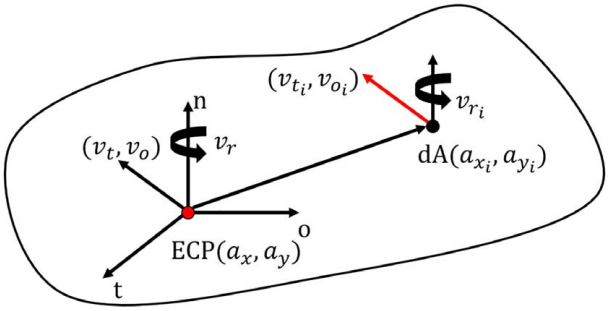

Fig. 4 Notation for planar sliding motion

a_x), where (a_x, a_y) are the x and y coordinates of the ECP and (a_{xi}, a_{yi}) are the x and y coordinates of a point on the patch. Substituting the above in Eq. (6) and simplifying, we obtain

$$P_c = -\left[\int_A v_t \beta_{ti} dA + \int_A v_o \beta_{oi} dA + \int_A v_{ri} \beta'_{ri} dA\right] \tag{7}$$

where $\beta'_{ri} = \beta_{ri} - \beta_{ti}(a_{yi} - a_y) + \beta_{oi}(a_{xi} - a_x)$. By noting that $\int \beta_{ti} dA = \lambda_t$, $\int \beta_{oi} dA = \lambda_o$, $\int \beta'_{ri} dA = \lambda_r$, where λ_t, λ_o are the components of net tangential forces at the ECP, and λ_r is the net moment about the axis normal to the contact patch and passing through the ECP, the power dissipation over the entire contact patch is given by $P_c = -(v_t\lambda_t + v_o\lambda_o + v_r\lambda_r)$. For specifying a friction model, we also need a law or relationship that bounds the magnitude of the friction forces and moments in terms of the magnitude of the normal force [43]. Here, we use an ellipsoidal model for bounding the magnitude of tangential friction force and friction moment. This friction model has been previously proposed in the literature [14,22,33,43] and has some experimental justification [44]. Thus, the contact wrench is the solution of the following optimization problem:

$$\begin{aligned} \max \quad & -(v_t\lambda_t + v_o\lambda_o + v_r\lambda_r) \\ \text{s.t.} \quad & \left(\frac{\lambda_t}{e_t}\right)^2 + \left(\frac{\lambda_o}{e_o}\right)^2 + \left(\frac{\lambda_r}{e_r}\right)^2 - \mu^2\lambda_n^2 \le 0 \end{aligned} \tag{8}$$

where the magnitude of contact force and moment at the ECP, namely, λ_t, λ_o, and λ_r are the optimization variables. The parameters, e_t, e_o, and e_r are positive constants defining the friction ellipsoid,and μ is the coefficient of friction at the contact [44,45]. As stated earlier, we use the contact wrench at the ECP to model the effect of the entire distributed contact patch. Note that there is *no assumption made on the nature of the pressure distribution between the two surfaces*. A key aspect of this work, which is different from the previous effort, is that here we consider that the normal force can be a function of the contact surface area. We will elaborate on how this is done within the context of the discrete-time framework since this requires that we identify the contact surface as part of our dynamic simulation algorithm.

Using the Fritz–John optimality conditions of Eq. (8), we can write [46]

$$\begin{aligned} 0 &= e_t^2\mu\lambda_n v_t + \lambda_t\sigma \\ 0 &= e_o^2\mu\lambda_n v_o + \lambda_o\sigma \\ 0 &= e_r^2\mu\lambda_n v_r + \lambda_r\sigma \\ 0 &\le \mu^2\lambda_n^2 - \lambda_t^2/e_t^2 - \lambda_o^2/e_o^2 - \lambda_r^2/e_r^2 \perp \sigma \ge 0 \end{aligned} \tag{9}$$

where the scalar σ is a Lagrange multiplier corresponding to the inequality constraint in Eq. (8).

5 Modeling for Tumbling Microrobots

As shown in Fig. 1, the magnetic microscale tumbling robot (μTUM) presented in this paper is cuboid-shaped and embedded with magnetic particles. The robot's magnetic features are aligned along a certain direction, and optimally it should be aligned along the lengthwise direction of the robot. An alignment offset angle is defined when there exists an angular difference between the actual alignment direction and the desired alignment direction.

There exists one magnetic field which rotates counterclockwise about the x-axis of the world frame. When the magnetic alignment of the field differs from that of the robot, a magnetic torque is applied to the robot until it is realigned with the field. Therefore, a rotating magnetic field causes the robot to rotate about the same axis. As shown in Fig. 1, if the robot is resting on the surface, the rotating field causes the tumbling motion of the robot, i.e., the robot will move forward by continuously flipping end-over-end. The magnetic torque $\mathbf{T}_m \in \mathbb{R}^3$ applied to the microrobot is

$$\mathbf{T}_m = V_m \mathbf{E} \times \mathbf{B} \tag{10}$$

where scalar V_m, vector $\mathbf{E} \in \mathbb{R}^3$ (the blue dashed lines in Fig. 3), and vector $\mathbf{B} \in \mathbb{R}^3$ are the magnetic volume, the magnetization, and the magnetic field strength of the robot, respectively. The direction of the adhesive force between the robot and the surface, λ_a, is along the negative direction of the contact normal, $\mathbf{n}$, and its value depends on the material of the object (we use scalar C to denote the coefficient of adhesive force between robot and surface) and the area of contact region $A_{contact}$. The expression for λ_a is

$$\lambda_a = CA_{contact} \tag{11}$$

Newton–Euler Equations for Tumbling Microrobot: As shown in Fig. 3, $\boldsymbol{\lambda}_{app} \in \mathbb{R}^6$ is the generalized applied force acting on CM of the robot and includes gravitational force mg, electrostatic force F_{elect}, adhesive force λ_a and magnetic torque $\mathbf{T}_m \in \mathbb{R}^3$. The contact wrench acting on the ECP includes normal contact force, λ_n, and frictional forces and moments, λ_t, λ_o and λ_r. The generalized velocity is $\mathbf{V} = [\mathbf{v}, \mathbf{w}]$. The Newton-Euler equations are

$$\mathbf{M}\dot{\boldsymbol{\nu}} = \mathbf{W}\begin{bmatrix} \lambda_n - \lambda_a \\ \lambda_t \\ \lambda_o \\ \lambda_r \end{bmatrix} + \begin{bmatrix} 0 \\ 0 \\ -(mg + F_{elect}) \\ \mathbf{T}_m \end{bmatrix} + \boldsymbol{\lambda}_{vp} \tag{12}$$

where the mapping matrix $\mathbf{W} = [\mathbf{W}_n, \mathbf{W}_t, \mathbf{W}_o, \mathbf{W}_r] \in \mathbb{R}^{6\times4}$ is computable based on Eq. (2). The magnetic torque $\mathbf{T}_m$ is based on Eq. (10). The adhesive force λ_a is in the opposite direction of the normal force λ_n, and its value is computed by the Eq. (11). Please note that Eq. (12) is a system of six differential equations.

Discrete-Time Dynamic Model: We use a velocity-level formulation and an Euler time-stepping scheme to discretize the above system of equations. Let superscript u be the beginning of current time-step, $u+1$ be the end of current time-step, and h be the time-step length. After letting $\dot{\mathbf{V}} \approx (\mathbf{V}^{u+1} - \mathbf{V}^u)/h$ and impulse $p_{(.)} = h\lambda_{(.)}$, we get the following discrete-time system. The system of equations in general is a mixed nonlinear complementarity problem. The vector of unknowns, $\mathbf{z}$, can be partitioned into $\mathbf{z} = [\mathbf{u}_z, \mathbf{v}_z]$, where

$$\mathbf{u}_z = [\mathbf{V}; \mathbf{a}_1; \mathbf{a}_2; p_t; p_o; p_r], \quad \mathbf{v}_z = [\mathbf{l}_1; \mathbf{l}_2; \sigma; p_n]$$

The equality constraints in the mixed NCP are as follows:

$$\mathbf{M}^u(\mathbf{V}^{u+1}-\mathbf{V}^u)=\mathbf{W}^{u+1}\begin{bmatrix}p_n^{u+1}-p_a^u\\ p_t^{u+1}\\ p_o^{u+1}\\ p_r^{u+1}\end{bmatrix}-\begin{bmatrix}0\\ 0\\ mgh+p_{elect}\\ -\mathbf{T}_m^u h\end{bmatrix}-\mathbf{p}_{vp}^u$$

$$0=\mathbf{a}_1^{u+1}-\mathbf{a}_2^{u+1}+l_k^{u+1}\mathcal{C}(\mathbf{F},\mathbf{a}_1^{u+1})$$

$$0=\mathcal{C}(\mathbf{F},\mathbf{a}_1^{u+1})+\mathcal{C}(\mathbf{G},\mathbf{a}_2^{u+1})$$

$$0=\mu e_t^2 p_n^{u+1}\mathbf{W}_t^{Tu+1}\mathbf{V}^{u+1}+p_t^{u+1}\sigma^{u+1}$$

$$0=\mu e_o^2 p_n^{u+1}\mathbf{W}_o^{Tu+1}\mathbf{V}^{u+1}+p_o^{u+1}\sigma^{u+1}$$

$$0=\mu e_r^2 p_n^{u+1}\mathbf{W}_r^{Tu+1}\mathbf{V}^{u+1}+p_r^{u+1}\sigma^{u+1} \tag{13}$$

The complementarity constraints on $\mathbf{v}_z$ are as follows:

$$0\le\begin{bmatrix}\mathbf{l}_1^{u+1}\\ \mathbf{l}_2^{u+1}\\ \sigma^{u+1}\\ p_n^{u+1}\end{bmatrix}\perp\begin{bmatrix}-\mathbf{f}(\mathbf{a}_1^{u+1})\\ -\mathbf{g}(\mathbf{a}_2^{u+1})\\ \xi\\ \max\mathbf{f}(\mathbf{a}_2^{u+1})\end{bmatrix}\ge 0 \tag{14}$$

where

$$\xi=(\mu p_n^{u+1})^2-(p_t^{u+1}/e_t)^2-(p_o^{u+1}/e_o)^2-(p_r^{u+1}/e_r)^2$$

Furthermore, the adhesive impulse p_a^u is required as input at the beginning of each time-step. We can compute p_a^u based on Eq. (11). However, in order to compute p_a^u, we need to know the contact area at each time-step. However, this is not part of our solution to the dynamic model. In the next section, we discuss the procedure to compute the contact area, $A_{contact}$.

Computing the Area of Contact Region: In general, the area of the contact region, $A_{contact}$, depends on the geometry and configurations of objects in contact, which is hard to describe mathematically. However, in our case, the contact happens between the microrobot (μTUM) and the planar surface. The contact region is the side of the robot in contact with the surface. The geometry and dimension of the robot can be measured a priori, and we can compute the area of each side of the robot. The ext question is which side of the robot is in contact at the current time?

The question can be answered by utilizing the Lagrange multipliers of contact constraints. Based on the complementary condition, once $l_i^{u+1}>0$, its associated constraint $f_i(\mathbf{a}_1^{u+1})=0$, i,e., the ECP should lie on the constraint or side i. If $p_n^{u+1}>0$, which indicates the robot has contact on the surface at the end of the current time, the active constraint or side i will be the side of the robot that has contact with the surface.

To sum up, first, we can compute the area of each side of the robot based on the knowledge of the robot's geometry and dimensions. Then, we solve the discrete-time model at each time-step. The solutions for l_i^{u+1} and p_n^{u+1} will be utilized to identify the side or boundary of the robot in contact and return us $A_{contact}^{u+1}$. Eventually, based on Eq. (11), we compute adhesive impulse p_a^{u+1}, which would be used as input for the next time-step. In the subsequent sections, we will utilize the method in the simulation to estimate the effect of adhesion.

6 Dynamic Model Validation

To validate our dynamic model, we compare our simulation results to experimental results. We use the following experimental tests: (i) tumbling locomotion tests on paper, (ii) inclined plane traversal tests on paper, and (iii) inclined plane traversal tests on aluminum. In the tumbling locomotion tests, the μTUM moves on a flat horizontal surface, and we use the average translational speed, v, in the desired direction of motion as the metric. In inclined tests, we measure the maximum climbable incline angle, φ, of the microrobot. We perform the tests in the simulation and validate the results with experiments. We will first discuss the experimental setup and then discuss the results of the three tests.

6.1 Experimental Setup. The microrobots used in the experiments described in this section are composed of two SU-8 polymer ends doped with magnetic NdFeB particles and a non-magnetic middle section that is entirely made up of SU-8 polymer. Their external dimensions are as follows: length, $L=0.8\times10^{-3}$ m, width, $W=0.4\times10^{-3}$ m, and height, $H=0.1\times10^{-3}$ m. The microrobots were fabricated using a two-step photolithography process described in Ref. [8]. Two different generations of microrobots were used in the experiments. The material properties for the first generation are listed in Table 1, and they were used for the experiments on paper. The material properties for the second generation are listed in Table 3, and they were used for the experiments on aluminum. The second-generation robots underwent an additional step where they were exposed to a 9 T uniform magnetic field generated by a PPMS machine (Quantum Design) after the SU-8 curing process. This field was strong enough to realign the embedded NdFeB particles homogeneously within the cured SU-8, and the resulting magnetization was approximately three times larger than earlier tumbling microrobot iterations.

A system of eight electromagnetic coils (MFG-100 system, MagnetibotiX AG) was used to generate the rotating magnetic field that actuates the microrobots. Figure 5 depicts the experimental setup. While the microrobots used for the experiments have three distinct sections, our simulation simplifies them into single, homogeneous blocks of uniform mass distribution. We argue this assumption is acceptable at the microscale, where factors such as weight and inertia are much smaller in magnitude than factors proportional to distance and surface area, such as adhesion and electrostatic forces.

Several properties utilized in the simulation were derived from physical measurements of related parameters. To obtain the adhesion coefficient for the substrate of interest, the microrobot was laid flat over the substrate in dry air. The external magnetic field was set to a static vertical orientation, and the field strength was incrementally increased from zero until the microrobot started rotating upward. The field strength at which rotation occurred was used to calculate the magnetic torque that counteracted the adhesion force resisting upwards motion. Dividing this torque by the moment arm and by the total contact surface area of the robot resulted in the adhesion coefficient for that substrate. To estimate the friction coefficient, a wafer of SU-8 was placed over a sheet of the substrate of interest in dry air. The SU-8 side of the wafer was placed in contact with the substrate and 20 g of additional mass was attached to the other side, ensuring that the dominant force between the microrobot and the substrate would be measured instead of adhesion or electrostatic forces. The substrate was then tilted from a horizontal position until the wafer started slipping downwards. The angle at which slippage occurred was noted, and the friction coefficient for the substrate was approximated by taking the tangent of this angle.

Table 1 Parameters for μTUM on paper

Description	Value	Units
Mass (m)	3.78×10^{-8}	kg
Electrostatic force (F_{elect})	6.54×10^{-7}	N
Friction coefficient (μ)	0.3	–
Magnetic alignment offset (α)	27	deg
Magnetic volume (V_m)	2.9×10^{-11}	m^3
Magnetization (|**E**|)	15,000	A/m
Coefficient of adhesion force (C)	1.19	N/m^2

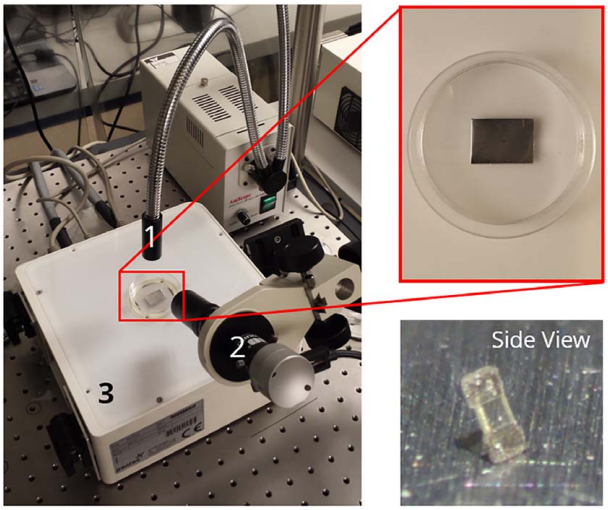

Fig. 5 Experimental setup with (1) halogen lamp, (2) side camera, and (3) MFG-100 system. Additional images show an aluminum surface inside a petri dish at the center of the workspace and a side view of the μTUM as seen through the camera.

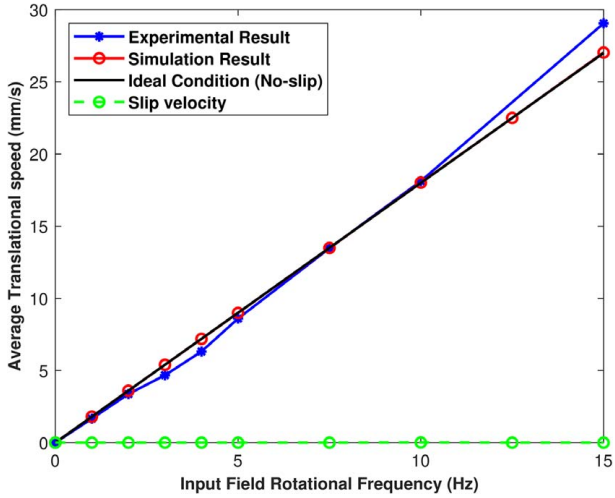

Fig. 6 Tumbling locomotion tests on paper (10 mT field)

6.2 Tumbling Locomotion Tests on Paper. The first scenario investigated is for tumbling locomotion of the μTUM traversing a dry paper substrate. The parameters are again listed in Table 1. As listed in the table, the coefficient of adhesion force is $C = 1.19\ \text{N/m}^2$. Thus, the effect of adhesion between the robot and paper can not be ignored. Therefore, in our simulation, we take the adhesive force into account and compute the value based on our dynamic model. The simulation is performed in order to evaluate the robot's performance on the substrate under varying field rotation frequencies. If the robot tumbles without slipping on the rough paper surface, the robot's average translational speed, v, should be approximately equal to two times the sum of body length and body height $(L+H)$ multiplied by the field rotational frequency f_{rot} [8]:

$$v = 2(L+H)f_{rot} \tag{15}$$

We applied a rotating magnetic field of 10 mT to the robot. The initial configuration the robot is $\mathbf{q} = [0, 0, q_z, 1, 0, 0, 0]^T$, where the z-axis height of the CM $q_z = 100\ \mu\text{m}$. The initial generalized velocity $\mathbf{V}$ is zero. As shown in Table 1, the magnitude of mass (m) and volume (V_m) is small, which is in the order of 1e–8 kg and 1e–11 m^3. To increase the accuracy in our simulations, we set the tolerance to be 1e–10. Furthermore, we scale up the metric units. In the simulations, the unit for mass is grams (g), and the unit for distance is millimeters (mm).

Figure 6 compares the experimental and simulation results with the ideal no-slip solution (Eq. (15)). The simulation results match reasonably well with the experimental results up to the frequency of 10 Hz. Furthermore, the simulation results also match with the ideal solution since there is no slip at the contact during the tumbling motion (the slip velocity plotted in Fig. 6 is almost zero and is visually indistinguishable from the x-axis). At the frequency of 15 Hz, the experimentally obtained average velocity is higher than expected due to complications in the MagnebotiX machine producing the external magnetic field. It is suspected that stray field gradients become more prominent at higher rotational frequencies and pull the microrobot toward the edges of the workspace, causing it to move faster.

6.3 Inclined Plane Traversal Tests on Paper. In the second scenario, the simulation is used to determine whether the designed microrobot can climb an inclined surface (paper in dry conditions) at various angles. We applied a 20 mT rotating magnetic field and 1 Hz frequency to the robot. We compared the simulation results with experimental results to validate our model. In this scenario, we again take the adhesive force into account in the simulation. The results are reported in Table 2. Based on the experimental result, the robots can go over a maximum inclination of 45 deg on paper, but it will fail to climb a slope of 60 deg. The simulation output matches these results. Figure 7(*a*) plots the adhesive force when the robot is tumbling over the incline at 45 deg. It can be observed from this figure that the force changes periodically, depending on the contact surface. When the contact area is large (length × width), the adhesive force reaches a value of 3.8e − 7 N. When the contact area is small (width × height), the adhesive force value goes to 4.7e − 8 N. In line contact cases, the adhesive force is almost zero. Figure 7(*a*) also plots the magnitude of the frictional force. We notice that the frictional force mostly stays constant during the motion. The value oscillates slightly when the value of adhesive force changes. To explain the phenomena, in Fig. 7(*b*), we plot the magnitude of the net external torque, which is the sum of the torques due to the magnetic field and normal force. Note that when the net external torque is equal to zero, the robot will tumble forward with constant velocity, and the frictional force will stay constant. When the net external torque is greater than zero, the robot will accelerate or decelerate, and the value of the frictional force will increase or decrease accordingly to balance the inertial force. As validated by Fig. 7(*b*), we observe that the timings of the jump in frictional force correspond to the timings where there is a jump in the net external torque (there are small jumps near the 0, 1, and 2-second mark that are hard to see at this scale).

Table 2 Inclined plane tests on paper (20 mT @ 1 Hz)

Incline (φ)	Simulation (Y/N)	Experiment (Y/N)
5 deg	Y	Y
10 deg	Y	Y
15 deg	Y	Y
30 deg	Y	Y
45 deg	Y	Y
60 deg	N	N

6.4 Inclined Plane Traversal Tests on Aluminum. In our third scenario, we analyze the performance of a μTUM with improved magnetic properties. In Table 3, the magnetization of the newer μTUM's (51,835 A/m) is much higher than that of original

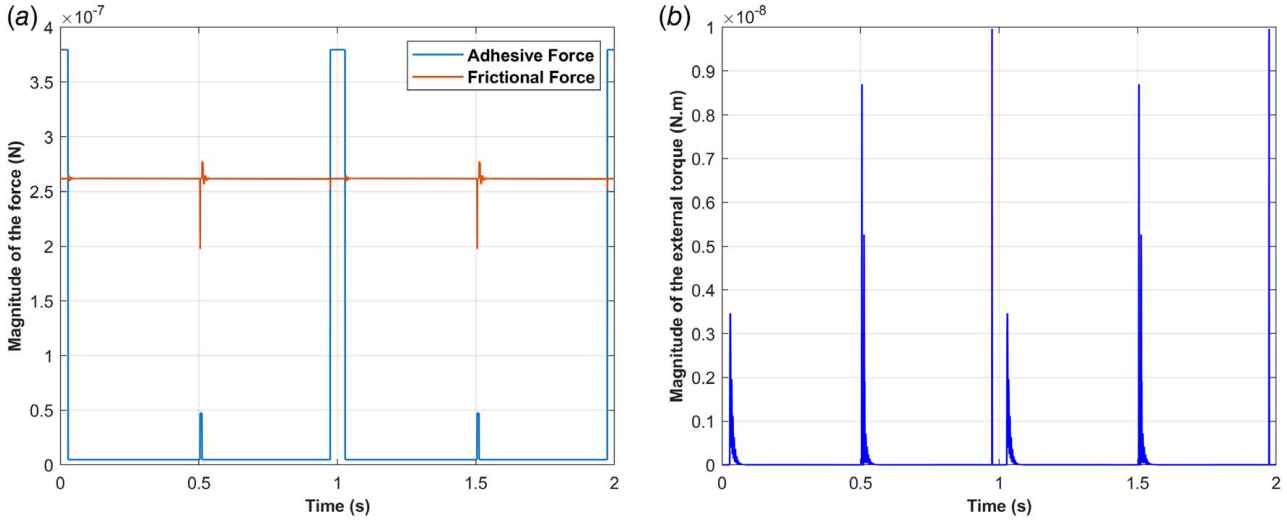

Fig. 7 Simulation result for the magnitude of (*a*) adhesive force, frictional force and (*b*) the net external torque (sum of the torque due to magnetic field and normal force) acting on μTUM robot when it is tumbling over the incline (paper) of 45 deg (20 mT field at 1 Hz)

μTUM (15,000 A/m). Furthermore, the newer μTUM has zero magnetic alignment offset angle. The inclined tests are performed on aluminum, which is non-magnetic and conductive. Therefore, there should not be any significant electrostatic force or additional magnetic force acting on the robot when it is tumbling over the substrate. Although an electromagnetic drag force may be exerted on the μTUM due to eddy currents induced in the conductive aluminum, this force is estimated to be two orders of magnitude smaller than the magnetic torque and thus negligible. The coefficient of adhesive force on aluminum was found to be 26.18 N/m^2, and the coefficient of friction was found to be 0.54. These values are almost seven times more than the case for paper. Therefore, we must also consider this adhesive force in our simulation. The procedure for obtaining the parameters is stated in our Sec. 6.1. We applied a 20 mT rotating magnetic field at 1 Hz frequency to the robot. The result of inclined plane climbing tests is reported in Table 4. In both the simulations and the experiments, the robot can successfully climb the inclination of 30 deg but fails to climb it at 45 deg.

7 Dynamic Simulation-Based Microrobot Design

Now that the simulation model has been validated, it can be used to explore alternative μTUM geometries for improved mobility. The priority for these new geometries is reducing or eliminating area contact during the tumbling cycle and decreasing the minimum actuation torque necessary to counteract adhesion force. This change can be implemented by altering the side profile of the microrobot and including spiked or curved features to prop the microrobot above the substrate surface. As shown in Fig. 8, we simulated (*a*) spiked-shaped robots (SS), (*b*) robots with spiked ends (SES), (*c*) curved-shaped robots, and (*d*) the cuboid-shaped μTUM robots from before. To explore the effect of the robots' design and dimensions on their performance, we assume all the robots have the same geometry-independent properties listed in Table 3, such as friction coefficient, magnetization, and coefficient of adhesion force. The geometry-dependent properties such as mass, magnetic volume, and moment of inertia change between designs. The simulation includes both the tumbling locomotion tests and the inclined plane traversal tests from before. For each robots' design, the tests are performed once in the simulation. Since the microrobot moves on the paper or on the aluminum, we consider the adhesive forces in our simulation.

Table 3 Parameters for improved μTUM on aluminum

Description	Value	Units
Mass (m)	4.44×10^{-8}	kg
Electrostatic force (F_{elect})	0	N
Friction coefficient (μ)	0.54	–
Magnetic alignment offset (α)	0	deg
Magnetic volume (V_m)	3.2×10^{-11}	m^3
Magnetization (|**E**|)	51835	A/m
Coefficient of adhesion force (C)	26.18	N/m^2

Table 4 Inclined plane tests on aluminum (20 mT @ 1 Hz)

Incline (φ)	Simulation (Y/N)	Experiment (Y/N)
30 deg	Y	Y
45 deg	N	N

In the tumbling locomotion tests, we applied a 20 mT rotational magnetic field at 10 Hz frequency to all the robots. Although these tests could have been performed at 1 Hz for consistency, we increased this value to 10 Hz in order to emphasize the velocity differences between the four designs due to slip. Initially, all robots stay at rest on the substrate surface. The initial configuration of each robot is $\mathbf{q} = [0, 0, q_z, 1, 0, 0, 0]^T$, where z-axis height of the CM, $q_z = 325$ μm for SS, $q_z = 275$ μm for SES, $q_z = 220$ μm for curved shape, and $q_z = 100$ μm for cuboid shape. The initial generalized velocity $\mathbf{V}$ is zero.

Figure 9 shows the displacement q_y of all the robots along the y-direction as the robots tumble forward on a paper substrate. We only present the plots for paper, since, each robot's performance on paper is similar to its performance on aluminum. Furthermore, the curved shape robot was found to move the fastest while the cuboid shape robot moved the slowest.

In the inclined plane traversal test, we chose the substrate to be aluminum. We let the vector of the initial configuration to be $\mathbf{q} = [0, 0, q_z/\cos(\varphi), \cos(\varphi/2), \sin(\varphi/2), 0, 0]^T$, where the inclined angle $\varphi = 20$ deg, 30 deg, 45 deg. All robots except the curved shape robot successfully climbed the incline up to 30 deg and failed to climb it at 45 deg. The result of inclined plane climbing tests is reported in Table 5. Based on the simulation results, we can conclude that the curved shaped robot performs best in terms of linear speed but is comparatively worse at climbing. In addition, we find that the basic cuboid shape robot is not the best design for

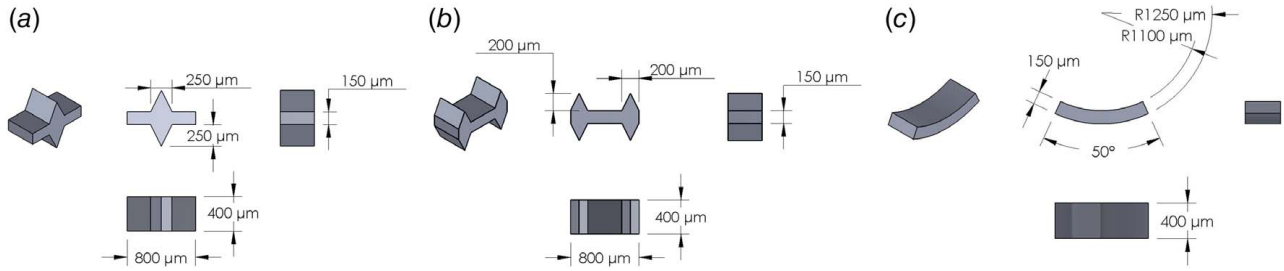

Fig. 8 Design and dimensions of μTUM robots with different geometric shapes: (*a*) spiked-shaped (SS) robot, (*b*) spiked ends-shaped (SES) robot, and (c) curved-shaped robot

tumbling locomotion. Instead, we found that robots with spiked ends geometry (SES) have the best overall performance in locomotion tests and inclined plane tests.

8 Manufacturing Alternative Microrobot Geometries

8.1 Manufacturing Methods and Considerations. To verify the results of the shape exploration process, we fabricated physical versions of the spike-shaped robots (SS) and spiked ends-shaped robots (SES) for further experimentation. Several manufacturing challenges and limitations, however, were encountered while producing these geometries.

While capable of fabricating precise designs within the nanometer range, photolithography is limited to patterning 2D designs over a flat substrate. Complex geometric features can only be patterned along one direction, and surfaces along other directions maintain a rectangular cross section. For the basic cuboid shape microrobot, the top plane (a 800 μm × 400 μm rectangle) is the face that is patterned during the photolithography process. To realize the more complex spike features, however, the side plane of the microrobot must be patterned instead. This requirement poses problems because the microrobot is much wider (400 μm) than it is tall (100 μm), necessitating a thicker SU-8 layer to pattern from. Spin-coating a single, uniform SU-8 layer thicker than 200 μm is a challenging and uncommon procedure, with multiple stacked SU-8 layers being the preferred alternative. However, this option is not available for magnetic microrobots. The embedded neodymium particles are opaque and block the vision of the preceding SU-8 layers underneath, making optical mask alignment difficult between separate SU-8 layers. An attempt was made to fabricate multiple cross-sectional slices of thin SU-8 layers and manually bind them together to form a completed microrobot. This process was prone to alignment errors between the slices due to its manual nature. It also led to rough edges on the resultant microrobots that impaired consistent motion. Additional difficulties were encountered while separating the patterned spiked SU-8 geometries from their silicon wafer substrates. The small feature size of the spikes, additional stress concentration points, and brittle nature of SU-8 made breakages common during microrobot extraction and handling operations.

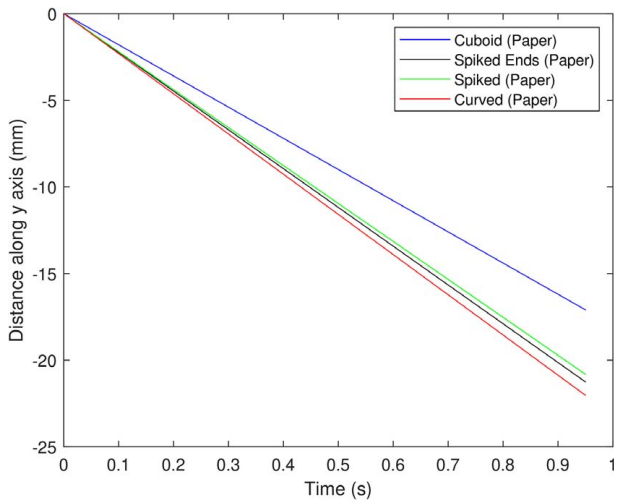

Fig. 9 Simulation result for tumbling locomotion tests (20 mT field at 10 Hz) for robots with different geometric shapes on paper. The result for the tests on aluminum are similar to the results on paper.

Table 5 Simulation results for robots with different geometric shapes: inclined plane tests on aluminum (20 mT @ 1 Hz)

Incline (φ)	Cuboid (Y/N)	Spiked (Y/N)	Spiked Ends (Y/N)	Curved (Y/N)
20 deg	Y	Y	Y	Y
30 deg	Y	Y	Y	N
45 deg	N	N	N	N

To circumvent these manufacturing challenges, we proposed an alternative method of fabricating the desired microrobot geometry. Instead of rigid SU-8 photoresist, more compliant, elastomeric PDMS (Polydimethylsiloxane, Sylgard 184) is used to make the microrobot more robust against fracture. While PDMS is generally considered to be a soft material, we argue that the applied loads are too small to yield significant deformation of the microrobot, and the simulation's rigid body assumption can be maintained. Unlike SU-8, PDMS cannot be patterned using photolithography and requires a mold or an alternative process to be shaped into the desired geometry. Since molds tend to produce burrs on the edges of the extracted geometry, which can result in erratic tumbling motion, we opted to use laser cutting to form the PDMS material instead.

Making laser cutting a viable fabrication option required additional alterations to the microrobot design to ensure clean cuts. The PDMS material can undergo excessive curing and become extremely brittle if the embedded neodymium particles absorb too much thermal energy and significantly raise the internal temperature. To avoid this problem, microrobots were patterned at half their intended size, and the mass ratio of embedded magnetic particles was reduced from 1:1 to ≈1:8.5. This particle reduction also lead to a proportional decrease in microrobot magnetization from 51,835 A/mto 18,661 A/m.

The fabrication process for the resultant spiked geometry microrobots (SES and SS) consists of the following steps: the PDMS is thoroughly mixed with the magnetic particles to remove air bubbles large enough to cause problems in the fabrication process. Then, the doped PDMS is placed on a glass microscope slide with a #2 glass cover slip (Fisher Scientific) on each side to set the layer thickness (400 μm). Another microscope slide is placed on top of the latter setup to keep the layer uniform at the

desired size. The microscope slides are held together using a binder clip on each side, and the entire system is placed on a hot plate at 90 °C for an hour and a half to cure the PDMS. Lastly, the thin film is removed from the glass, cut in the shape of the microrobots using a laser system, and then magnetized using the same process as the SU-8 microrobots (with a constant 9T magnetic field). For the cutting procedure, we utilize a custom laser cutter system consisting of a femtosecond laser (CARBIDE, 04-1000), beam expander (Thorlabs, BE02-050B), attenuator (Altechna, Watt Pilot), waveplate, Brewster type polarizer, and 20X objective lens (Mitutoyo, 0.42NA) [47].

8.2 Manufacturing Errors and Limitations. When fabricating the microrobots, there can be errors due to (1) deviation of the magnetic axis from the ideal (we call this error *magnetic misalignment* or *magnetization error*, see Fig. 10), and (2) imperfections in the geometry (geometric error) of the microrobots (see Fig. 11). The laser beam used in the cutting process has tapered edges that result in an inward draft angle on the geometry of the fabricated microrobots. Additionally, the spiked features of the microrobots make them more difficult to manually align and mount during the magnetization process, leading to potential alignment errors in magnetic polarization. These manufacturing errors may affect the motion of robots, and thus understanding the effects of the errors is important in designing the robots. The change in material from SU-8 to PDMS can also affect interactions between the microrobot and substrate. The friction and adhesion coefficients of PDMS against aluminum, for example, are both substantially higher than those for SU-8. The presence of these discrepancies can lead to unexpected tumbling trajectories and behaviors that were not predicted using the original simulation parameters.

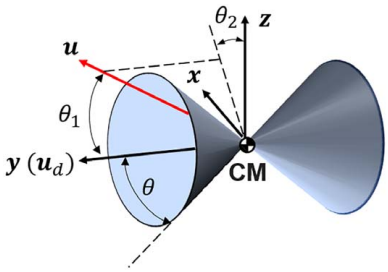

Fig. 10 Magnetization error: the possible deviations of the magnetic axis from the ideal is approximated by a double cone with an aperture $\theta = 10$ deg. The axis of the cone is the same as the *y*-axis of the robot, and the center of the cone is located at the robot's CM. The ideal magnetic axis, $\mathbf{u}_d \in \mathbb{R}^3$, coincides with the *y*-axis. The actual magnetic axis, $\mathbf{u} \in \mathbb{R}^3$, which is characterized by θ_1 and θ_2, lies on or within the cone.

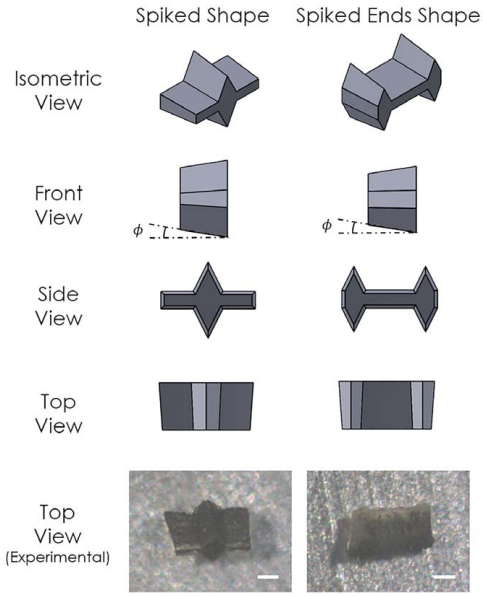

Fig. 11 Geometric error: the imperfections in the geometry of the manufactured microrobots with spiked shapes and spiked ends. The geometry of the laser-cut tapered edges is approximated by using an inward draft.

9 Incorporating Manufacturing Errors Into Dynamic Model

In this section, we perform simulation and experimental studies to understand the effects of the manufacturing errors.

9.1 Motion Prediction. PDMS was not observed to slip on aluminum substrates, regardless of incline angle, without large external loads. As a result, differences in incline climbing ability are minute between alternate designs of PDMS-fabricated tumbling microrobots. Therefore, we analyze the effects of the manufacturing errors and limitations by simulating their trajectory and speed on a flat surface instead. As shown in Fig. 10, we characterize the magnetization error with a double cone:

$$f_{cone}(\mathbf{u}) = \mathbf{u} \cdot \mathbf{u}_d - \cos(\theta) \leq 0 \tag{16}$$

where the vector $\mathbf{u}_d = [0, 1, 0]^T$ is the ideal magnetic axis, which coincides with the **y**-axis of the robot. The aperture of the cone is θ, and it is approximated as $\theta = 10$ deg. Due to the magnetization error, the actual magnetic axis $\mathbf{u} \in \mathbb{R}^3$ may deviate from $\mathbf{u}_d$, and it should lie on or within the cone. Thus, we use two parameters θ_1 and θ_2 to define the unit vector $\mathbf{u}$:

$$\mathbf{u} = [\sin(\theta_2)\sin(\theta_1),\ \cos(\theta_1),\ \cos(\theta_2)\sin(\theta_1)]^T$$

where $0 \leq \theta_1 \leq \theta$ and $0 \leq \theta_2 \leq 360$ deg. We define the inward draft angle, ϕ, to approximate the error in geometry of the microrobots, as shown in Fig. 11.

To analyze the effects of the manufacturing errors, we perform the tumbling locomotion tests in the simulation for the spiked-shape (SS) and spiked ends shape (SES) microrobots. The frequency of the magnetic field is chosen at 1 Hz, and the simulation time is 1s. In the analysis, we use the following metrics: (i) the angle of twist ϑ about the longitudinal axis of the robot after one cycle of motion, (ii) the drift d_e after one cycle of motion in the orthogonal direction to the direction of motion, and (iii) the average translational speed v along the desired direction of motion.

As shown in Fig. 12, the microrobots with manufacturing errors may twist without flipping or twist and flip to land on a side face during the tumbling motion. When the robot twists without flipping, we will say that the *robot twists* and when the robot twists and flips, we will say that the *robot flips*. We use the angle of twist after one cycle of motion, ϑ, to determine whether the robot twists or flips. When the robot twists (shown in Fig. 12(*b*)), the angle $-45\,\text{deg} \leq \vartheta \leq 45$ deg. When the robot flips (shown in Fig. 12(*c*)), the angle $\vartheta \geq 45$ deg or $\vartheta \leq -45$ deg. Additionally, there exists the drift, d_e, in the orthogonal direction to the direction of motion. Furthermore, when the robot twists or flips, the average tumbling speed, v, deviates from the ideal situation (without manufacturing errors). In the ideal situation (shown in Fig. 12(*a*)), the microrobot lands on the protruding spikes during the tumbling motion. Based on the dimensions of the robots, the speed v in the ideal situation for SS robots is 1093 μm/s, and for SES robots it is 1197 μm/s. When the microrobot flips (shown in Fig. 12(*c*)), it contacts the substrate on its side planes. The speed v of SS or SES depends on the length ($L = 400$ μm) and width ($W = 200$ μm) of this face. Based on Eq. (15), the speed v will be closer to 1200 μm/s.

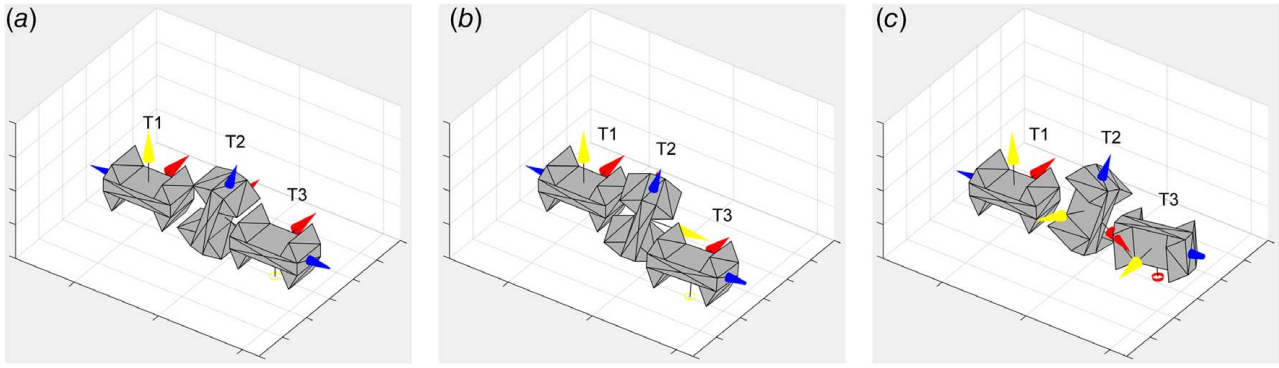

Fig. 12 The tumbling motion of the SES microrobot when it (*a*) moves as expected or (*b*) twists about the longitudinal axis of the body (the blue axis) with twist angle $-45\,\text{deg} \le \vartheta \le 45\,\text{deg}$ but falls on the spikes (as desired), (*c*) twists about the longitudinal axis of the body with angle $\vartheta \ge 45\,\text{deg}$ or $\vartheta \le -4\,\text{deg}$ to fall on a flat face with no spikes. (Note: T1, T2, and T3 correspond to instances in time with T1 < T2 < T3.)

Geometric Error Only: We first analyze the effect due to inward draft angle ϕ. The simulation results are shown in Fig. 13. In the simulations, we choose $\phi = 0\,\text{deg}, 1\,\text{deg}, \ldots, 15\,\text{deg}$, and the magnetic misalignment is assumed to be zero, i.e., ($\theta_1 = 0\,\text{deg}$, $\theta_2 = 0\,\text{deg}$). For each robot design, there are 16 simulation runs in total. Let us first analyze the results of SS microrobots. The trend of the angle of twist ϑ after one cycle of motion is shown in Fig. 13(*a*). In general, ϑ ranges from [−20 deg, 10 deg], which means that during motion, the robot always twists (without flipping). In the plot, initially the angle ϑ increases as ϕ increases, and it reaches the maximum value of $\vartheta = 10\,\text{deg}$ when $\phi = 13\,\text{deg}$. When $\phi = 14\,\text{deg}$, the angle becomes $\vartheta = 0\,\text{deg}$, which suggests that the robot does not twist during the motion. However, the robot does twist when it elevates on the spike, and it strikes on the flat surface after one cycle with twist angle $\vartheta = 0\,\text{deg}$. When $\phi = 15\,\text{deg}$, the robot strikes on the flat surface with $\vartheta = -21\,\text{deg}$ (in the opposite direction). The plot in Fig. 13(*c*) shows the trend for the drift d_e after one cycle. Note that when $\phi \ge 13\,\text{deg}$, the draft d_e starts decreasing. The reason could be when the angle ϑ is negative, the robot drifts in the opposite direction along the orthogonal axis. This causes the overall d_e to reduce. The trend for the speed v along the desired direction of motion is

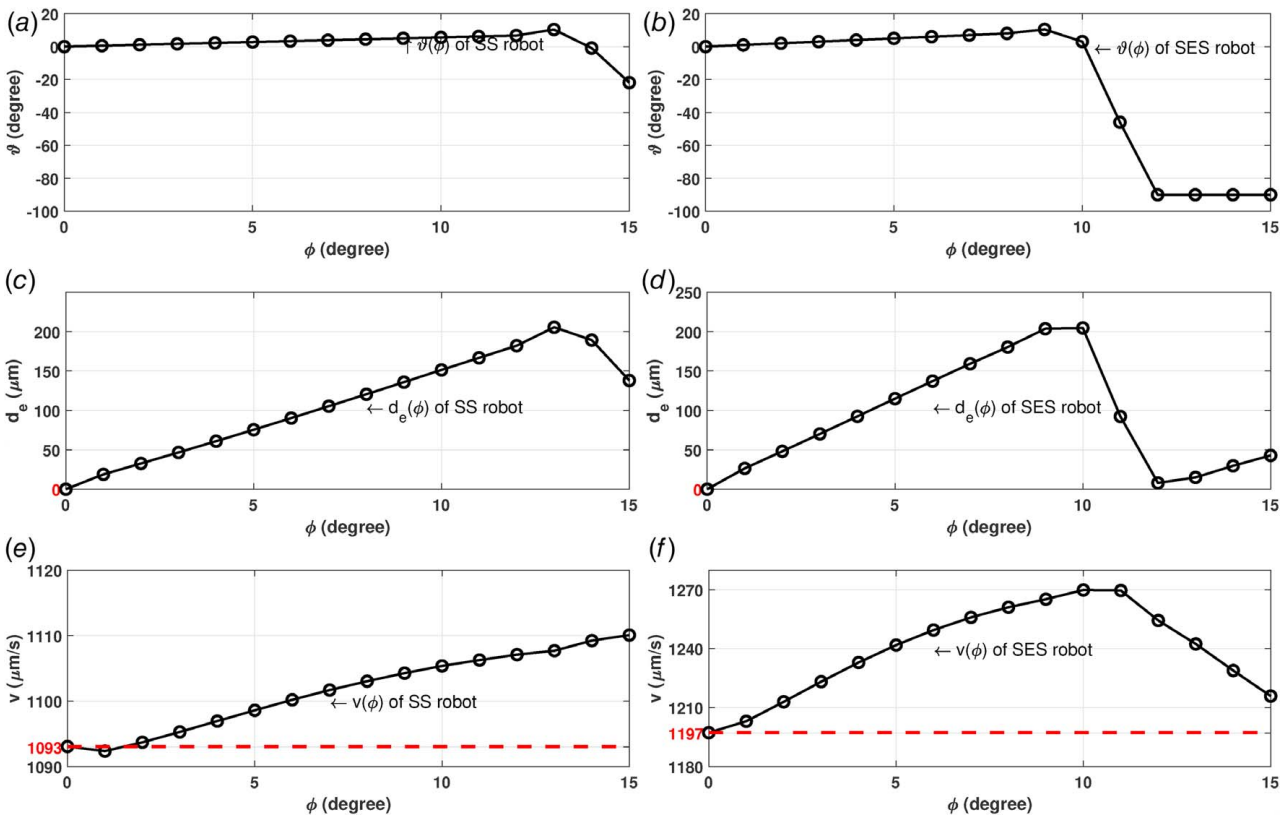

Fig. 13 The simulation results for locomotion tests at 1 Hz with geometric errors of an inward draft angle $\phi = 0\,\text{deg}, 1\,\text{deg}, \ldots,$ 15 deg. The simulation time is 1s. In all 16 simulation runs, the magnetization error is ignored ($\theta_1 = \theta_2 = 0\,\text{deg}$). The plots in the first column show the trends for SS microrobot of (*a*) angle of twist ϑ after one cycle of motion, (*c*) the drift d_e after one cycle, and (*e*) the average translational speed v. Similarly, the plots (*b*), (*d*), and (*f*) in second column show the results for SES robots. The values for the velocity in the ideal situation without manufacturing errors (shown in the dashed line) are given as v = 1093 μm/s and $v = 1197\,\mu$m/s, for the SS and SES designs, respectively.

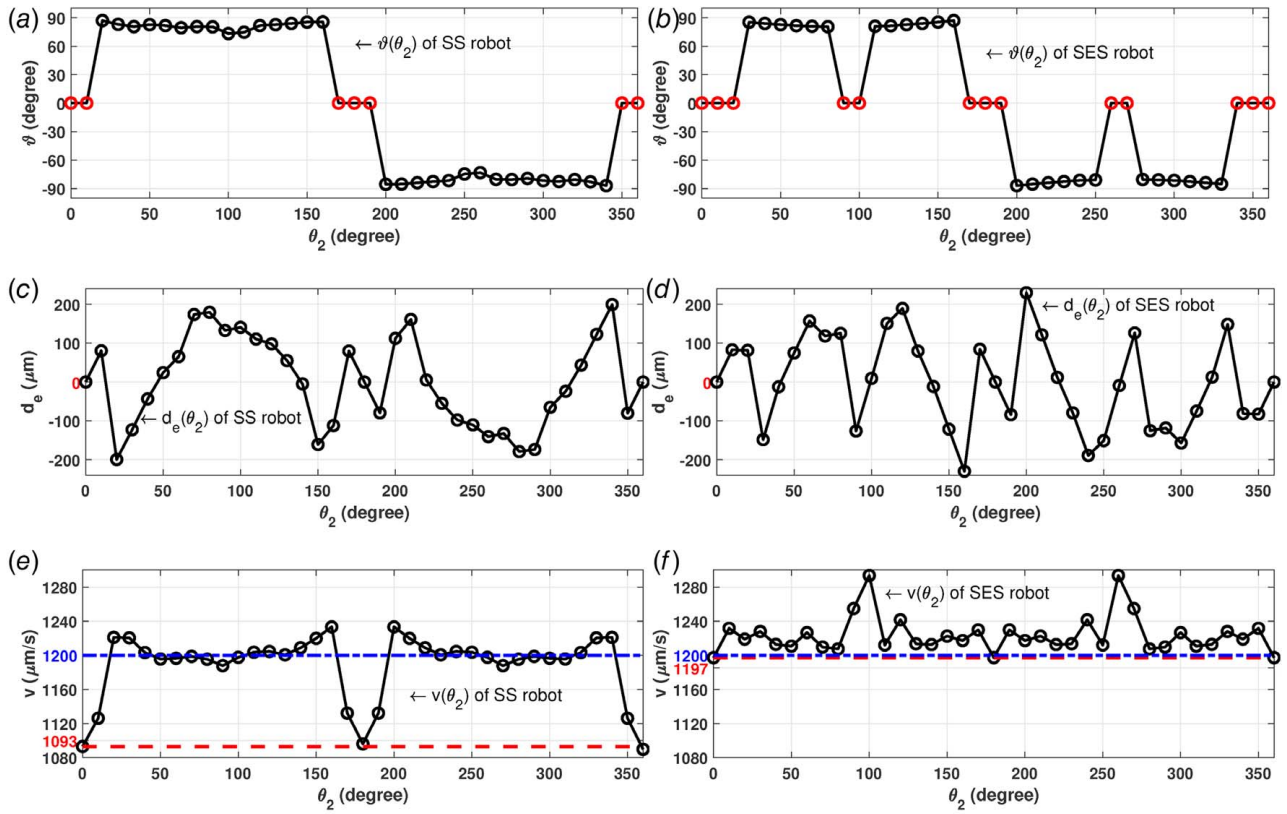

Fig. 14 The simulation results for locomotion tests at 1 Hz with magnetization error: $\theta_1 = 10$ deg and $\theta_2 = 10n$ deg, $n = 1, 2, \ldots, 36$ (the simulation with $\theta_1 = 0$ deg and $\theta_2 = 0$ deg are also included). In all 37 simulation runs, we ignore the imperfections in the geometry ($\phi = 0$ deg). The plots in the first column show the trends for SS microrobot of (*a*) angle of twist ϑ after one cycle of motion, (*c*) the drift d_e after one cycle, and (*e*) the average translational speed v. Similarly, the plots (*b*), (*d*), and (*f*) in second column show the results for SES robots. When the robot "flips," the value for the speed v is near 1200 μm/s (shown in the dash-dotted line).

shown in Fig. 13(*e*). The speed v of SS increases as the draft angle ϕ increases. We can conclude that the increase in draft angle ϕ will cause the SS robot to twist, which causes the speed of v and drift d_e to increase. Additionally, when $\phi \le 2$ deg, the drift can be relatively small: $|d_e| \le 50$ μm.

We then explore the result of the SES robot. In Fig. 13(*b*), the angle ϑ increases as ϕ increases up to 9 deg. Similar to the SS robot, when $\phi \ge 10$ deg, the angle ϑ of the SES robot starts reducing until it drops to -90 deg, indicating that the robot flips. In Fig. 13(*d*), the drift d_e drops to zero when $\phi \ge 12$ deg. In Fig. 13(*f*), the speed v decreases when $\phi \ge 12$ deg. We can conclude that the increase in draft angle ϕ will cause the SES robot to twist and eventually to flip. When the flip happens, the speed v starts to decrease as ϕ increases, and the drift d_e will start over from zero. For SES robots, the draft angle needs to be $\phi \le 1$ deg in order to achieve $|d_e| \le 50$ μm.

Magnetization Error Only: We now explore the effects only due to the magnetization error. As shown in Fig. 10, the error cone is characterized by θ_1 and θ_2. Here, we restrict the possible alignments to lie on the boundary of the cone, i.e., $\theta_1 = \theta =$ 10 deg. (When $\theta_1 = 5$ deg, the possible alignments lie within the error cone, which reduces the magnetization error in general. Due to lack of space, the results are not presented here.) There are 37 simulations runs for each robot, which includes the simulation with correct parameters ($\theta_1 = 0$ deg and $\theta_2 = 0$ deg) and simulations with magnetization error ($\theta_1 = 10$ deg and $\theta_2 = 10n$ deg, $n = 1, 2, \ldots,$ 36). We can observe that the plots for v in Fig. 14 are symmetric. This symmetry is due to the fact that the geometry of the robot is symmetric. As θ_2 increases, the magnetic alignment vector $\mathbf{u}$ rotates about the y-axis of the robot producing the symmetric nature of the plots.

Again, we start with the results for SS robots. Figure 14(*a*) show the trends for the angle of twist ϑ (y-axis) versus θ_2 (x-axis). When 20 deg $\le \theta_2 \le$ 160 deg or 200 deg $\le \theta_2 \le$ 340 deg, ϑ is almost 90 deg, i.e., the robot flips. Figure 13(*c*) illustrates the trends of the drift d_e along with the θ_2. It suggests that when θ_2 is near 50 deg, 140 deg, 220 deg or 310 deg, the drift $|d_e|$ can be smaller than 50 μm. However, all these cases are not preferred since the robot will flip in these instances. A detailed explanation of this behavior is provided in Sec. 10. Figure 14(*e*) shows the trend for speed v, and it illustrates that when the robot flips, the speed v jumps to nearly 1200 μm/s. We can conclude that the SS robots can tumble forward without flipping, when -10 deg $\le \theta_2 \le 10$ deg or 170 deg $\le \theta_2 \le$ 190 deg (the dots when $\vartheta = 0$ deg in Fig. 14(*b*)).

In the case of the SES robots, Fig. 14(*b*) shows that ϑ is almost zero when -20 deg $\le \theta_2 \le 20$ deg, 90 deg $\le \theta_2 \le 100$ deg, 170 deg $\le \theta_2 \le$ 190 deg, and 260 deg $\le \theta_2 \le$ 270 deg (red dots in Fig. 14(*b*)). In contrast, ϑ is almost 90 deg when ϑ is outside of these ranges. The trends of drift d_e and speed v are shown in Figs. 14(*d*) and 14(*f*) separately. When $\theta_2 = 100$ deg or $\theta_2 = 260$ deg, the velocity v increases to 1290 μm/s while the drift d_e continues to remain close to zero. Thus, the dynamic model suggests that the overall performance of the microrobots can potentially be improved by the presence of a draft angle.

Magnetization and Geometric Error: We now consider the joint effect of the magnetization error and imperfections in the geometry. Each robot shape is simulated in 592 different runs consisting of 37 magnetization profiles and 16 draft angles. The simulation results are shown in Fig. 15. In the plots, the x-axis is θ_2 and y-axis is ϕ. Each grid denotes the result of the simulation run with given θ_2 and ϕ, and the result is measured by the following metrics: the angle of twist ϑ, the drift d_e, or the speed v.

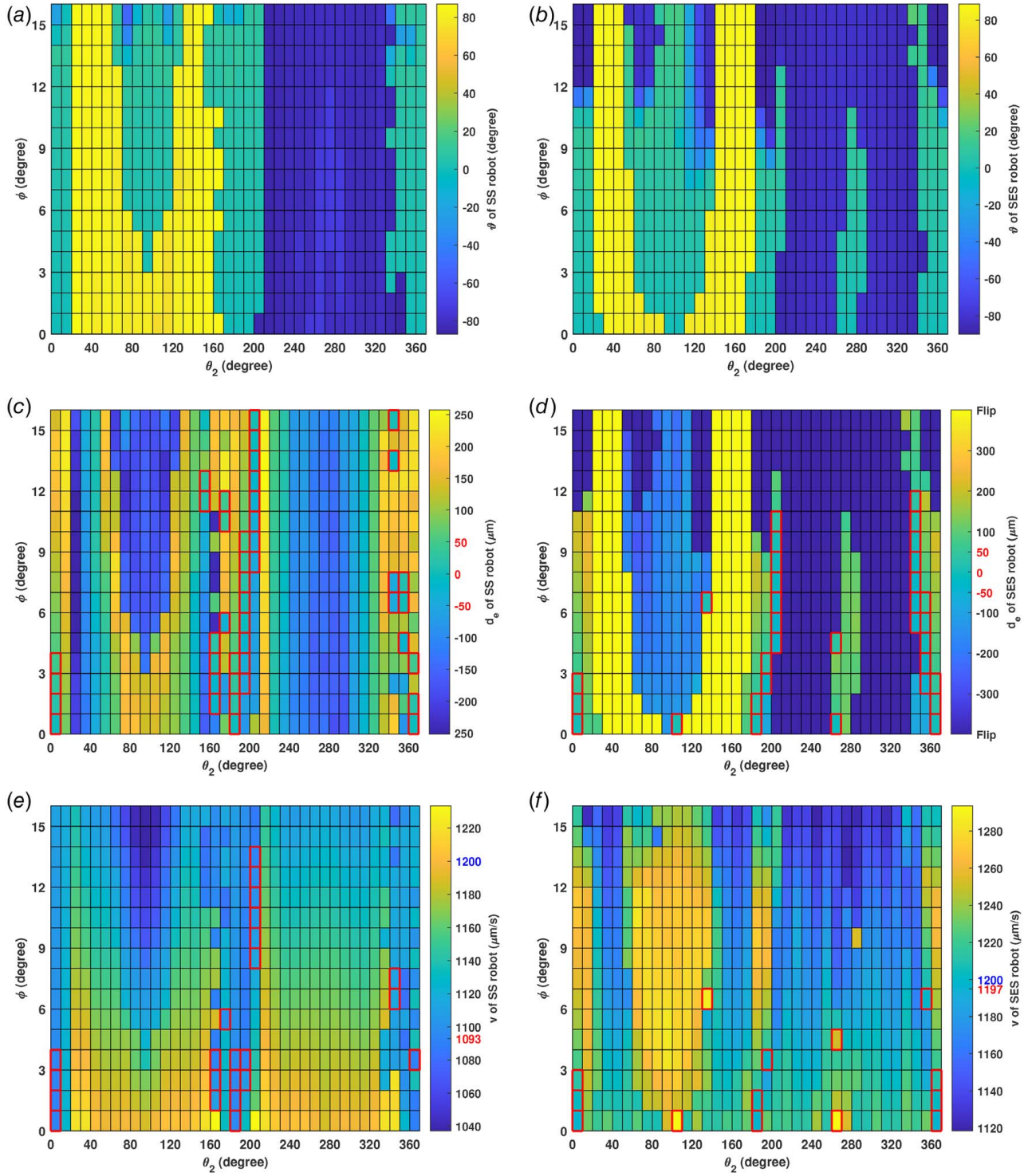

Fig. 15 The simulation results of tumbling locomotion tests at 1 Hz with manufacturing errors θ_2 and ϕ jointly. The plots in the first column show the distributions for SS microrobot of (*a*) angle of twist ϑ after one cycle of motion, (*c*) the drift d_e after one cycle, and (*e*) the average translational speed v. Similarly, the plots (*b*), (*d*), and (*f*) in second column show the results for SES robots. The grids with highlighted edges in (c) and (*d*) identify the cases that the robot does not flip and $|d_e| \leq 50\ \mu$m after one cycle. Based on the chosen cases, the grids in (e) and (f) further identify the cases with the additional condition that the speed v of the robot is higher than the velocity in the ideal situation. In the colorbars of (e) and (*f*), the value of velocity in an ideal situation is equal to 1093 μm/s and 1197 μm/s, and the velocity in the situation of flipping both equals 1200 μm/s.

For the SS robot, Fig. 15(*a*) shows the distribution for the angle of twist ϑ. When the robot flips, the angle of twist's value is $\vartheta \approx 90$ deg or $\vartheta \approx -90$ deg. Based on the plot, we can find the situations where the robot tumbles without flipping. Figure 15(*c*) illustrates the distribution of the drift d_e. The highlighted edges of the cells are used to identify the cases where the robot moves without flipping and with $|d_e| \leq 50\ \mu$m after one cycle. In accordance with intuition, we see that the manufacturing errors in general cause the SS robots to drift or even flip. When both geometric and magnetization errors are small, the SS robots tend to move as desired. In some

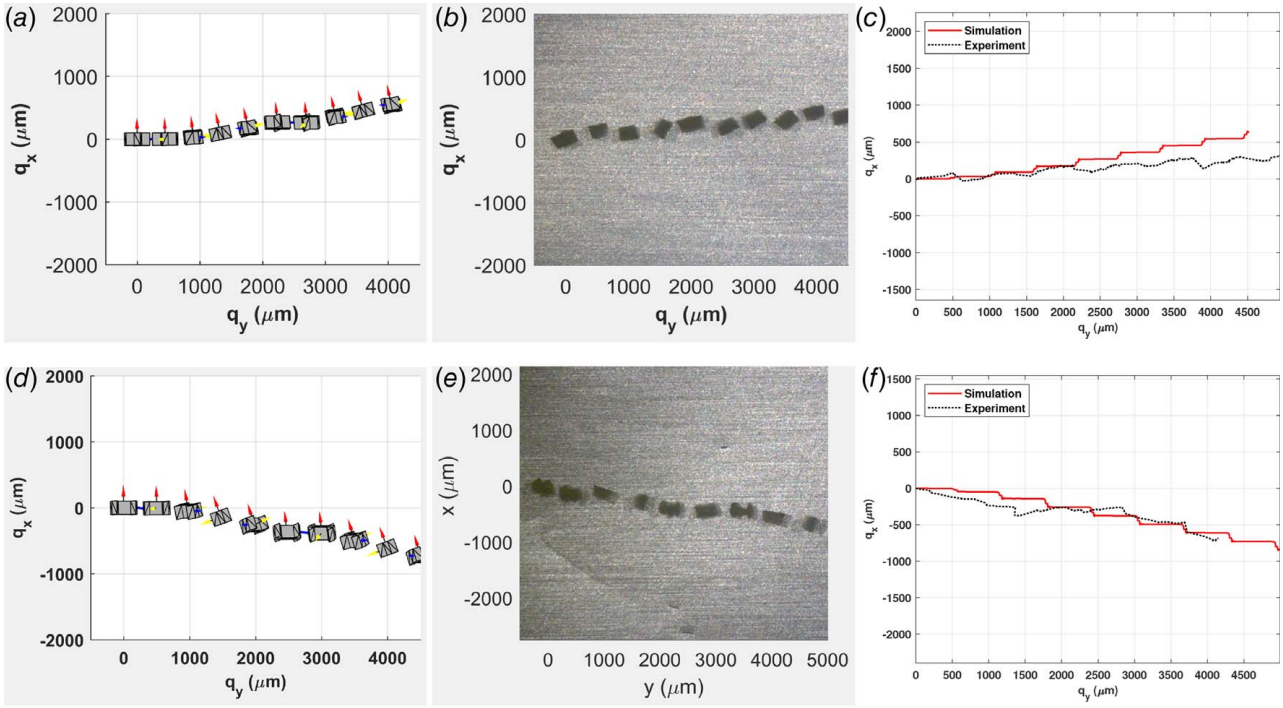

Fig. 16 Trajectories of microrobots at 1 Hz for one trial of locomotion tests on aluminum. The time for the simulation and the experiment is 4s. The first row shows the results for a SS microrobot, which includes: top view from the (*a*) simulation and (*b*) experimental results, and (c) comparison between the simulated and experimental trajectories for the X versus Y position of the microrobot. Similarly, the plots (*d*), (*e*), and (*f*) show the results for an SES microrobot.

instances when geometric (ϕ) or magnetization errors (θ_2) are not small (e.g., the situation when $\phi = 15$ deg and $\theta_2 = 200$ deg), the SS robots can still move as desired. Figure 15(*e*) illustrates the distribution of speed v for the SS robot. We find that the speed v can have higher values when the SS robot flips. This is expected since the speed for a flipped SS robot (1200 μm/s) is much higher than the ideal speed (1093 μm/s). We use highlighted edges to further identify the cases with the extra condition when the speed v is higher than the velocity in an ideal situation (1093 μm/s for the SS robot). These cases can be identified when both the manufacturing errors are small. Additionally, we notice that sometimes these cases are also identified when manufacturing errors are large (e.g., $\theta_2 = 200$ deg and 8 deg $\leq \phi \leq 14$ deg).

For the SES robot, the distributions of ϑ are shown in Fig. 15(*b*). Analogous to the plot for SS robots, the SES robots tend to flip when the manufacturing errors are high. In Fig. 15(*d*), the preferred cases for SES are also identified by the highlighted edges. This suggests that both the SS and SES robots have similar performance. The distributions of speed v for SES robots are shown in Fig. 15(*f*). We notice that the speed v is often higher when the SES robot twists without flipping. It is reasonable because when the robot flips, its speed (1200 μm/s) is almost the same as the ideal speed for the SES robot (1197 μm/s). When the robot twists without flipping, the speed v can be higher than the ideal speed. In Fig. 15(*f*), we use highlighted edges to identify the cases that satisfy the conditions that the SES robot does not flip, the drift $|d_e| \leq 50$ μm, and the velocity v is higher than the ideal speed as 1197 μm/s. Among the identified cases, we can find advantageous and non-intuitive design combinations.

9.2 Experimental Validation. After implementing the manufacturing errors into the dynamic model, we validate the simulation with experimental results. In both simulations and experiments, we execute the locomotion tests on the aluminum substrate. The manufacturing error of both the SS and SES microrobots used was $\theta_1 = 10$ deg, $\theta_2 = 0$ deg, and $\phi = 4$ deg. The frequency of the rotating magnetic field is at 1 Hz. The results are shown in Fig. 16. In the ideal situation, the microrobot should rotate about the rotating axis of the magnetic field (without loss of generality, we choose the x-axis) and tumble straight forward along the y-axis. When the manufacturing errors are taken into account, the snapshots of simulation in Figs. 16(*a*) and 16(*d*) show that the microrobot also drifts along the x-axis, and the trajectory does not follow a straight line. Furthermore, we notice that the robot starts to twist or even flip during the tumbling cycle, changing orientation along more than one rotational axis. We then run the experiment for the same locomotion test, and the results in Figs. 16(*b*) and 16(*e*) support what we have observed in the simulation. To explore and analyze further, we plot the x–y position of CM for the SS and SES microrobots in Figs. 16(*c*) and 16(*f*) separately. We can conclude that the trajectory in the experiment changes periodically, and the simulation matches with the experimental results with a similar pattern.

A video compilation of simulation and experimental results can be found online.[2]

10 Discussion

The intent of the alternative geometries analyzed in the previous two sections was to improve on the original cuboid geometry of the tumbling magnetic microrobots. By incorporating spiked protrusions or curved surfaces, the large faces of the microrobot would be elevated from the substrate, and area contact would be minimized, reducing the effect of resistive adhesive forces. Spiked geometry was further investigated after determining this design variant would lead to the best compromise between climbing ability and translational speed. Limitations in fabrication methods, however, led to unexpected behavior that brought additional benefits and drawbacks to the more complex geometry. In order to prevent the microrobots from fragmenting during the fabrication

[2]https://www.youtube.com/watch?v=NmxqMtOjyCg

process and during experimental handling, the constituent material was changed from doped SU-8 to doped PDMS. Laser cutting was also used instead of photolithography to allow thicker polymeric sheets to be processed. Feature size scale and magnetic particle concentration were both reduced to making laser cutting feasible. These changes resulted in critical differences in the motion of the new microrobots and their interaction with the substrate.

Strong adhesive forces between PDMS and aluminum in dry air allow PDMS tumbling microrobots to climb inclines much steeper than the 45° maximum inclination angle of comparable SU-8 counterparts. PDMS is also less brittle and fragile than SU-8, making PDMS microrobots robust against large applied loads and capable of including multiple stress concentration points without breakage. When manufacturing errors are minimized, spiked geometry microrobots do not encounter area contact during the tumbling cycle, reducing the minimum magnetic torques necessary to actuate the microrobots. In practice, fabrication through laser cutting introduces tapered edges that result in an inherent draft angle on the sides of the PDMS microrobots. Based on Fig. 13, larger draft angles generally result in increased translational velocities at the cost of a proportionally scaling drift away from the intended straight-line motion. Through the dynamic model, it is predicted that this drift can be kept at 50 μm or less when the draft angle ϕ is $\leq$2 deg or $\leq$1 deg for the SS robots and SES robots, respectively.

Manufacturing errors in the magnetization of the microrobots can occur regardless of their constituent material or geometry. These errors are introduced from the manual alignment and mounting of the microrobots during the magnetization process. SS and SES PDMS microrobots are more susceptible to misalignment than cuboid SU-8 variants due to their multiple protrusions and compressibility, making mounting difficult. The resulting misalignment leads to magnetic torques that cause rotation/twisting along with unintended directions. This problem is further compounded when draft angles are included, where point contact is frequent, and the microrobot has less resistance against spinning or flipping to the side. When considered in combination, it is estimated from the dynamic model that the absolute magnetization error should be kept at $|\theta_2| \leq 10$ deg, and the absolute draft angle at $|\phi| \leq 2$ deg in order to ensure the resulting microrobot drift is 50 μm or below.

Upon inspection of the simulation results in Figs. 13 and 14, there appear to be several advantageous parameter variations where velocity increases without a proportional increase in drift. In Fig. 14, for example, the SS robot's translational velocity increases to 1210 μm/s when the magnetization error θ_2 is 150 deg while the drift continues to remain close to zero. This behavior suggests that intentionally introducing manufacturing errors can potentially lead to better overall performance for the microrobot. It is important to point out, however, that the magnitude of the twist angle ϑ is greater than 45 deg in the majority of these disproportionate cases, and the microrobot tumbles in the "flip" orientation. This "flipped" tumbling orientation has a larger outer perimeter along with the side profile, resulting in higher translational speeds, but the microrobot also experiences significantly more area contact in this orientation. Instead of balancing over the spiked protrusions, as intended, the microrobot is periodically striking the substrate with the flat surfaces of its side planes. Due to the high adhesive forces between PDMS and aluminum, this frequent area contact may result in the microrobot getting stuck against the substrate, with the actuating torque not strong enough to counteract the increased adhesion. This effect is observed to occur in practice and should be considered in tandem with potential improvements in speed and drift. From Fig. 14, we also note that in one particular case, when the magnetization error θ_2 is 100 deg or 260 deg for the SES robot, the speed increases to 1290 μm/s with minimal drift and twisting introduced. Thus, through comprehensive variation of simulation parameters, advantageous but non-intuitive design combinations can be found. A caveat is that this advantage occurs when magnetization error is considered in the absence of geometric error. In practicality, there is often a mixture of non-zero magnetization and geometric errors.

While predictions from the simulation model do not match exactly with experimental results, the overall qualitative trends are similar between the two data sets. Without needing to spend significant time and resources on iterative physical prototyping of microrobots, new geometries and parameter variations can be rapidly analyzed to help find superior design combinations. Improved but non-intuitive combinations can be found, as discussed earlier, where introducing certain manufacturing errors could lead to potential improvements in performance. By estimating the manufacturing tolerances necessary to keep drift below a maximum level, the dynamic model can help determine whether minimizing magnetic alignment error or draft angle error is more cost-effective. The combination of PDMS material and laser cutting fabrication comes with limitations and drawbacks but also introduces a larger geometric design space from which to combat those faults. Our model is well-posed to reduce the resources necessary to explore this design space and make further improvements to microrobot design.

11 Conclusions

In this paper, we have demonstrated a dynamic simulation model that can account for intermittent non-point contact over multiple substrates and surface inclinations. We validated this model using experiments incorporating a tumbling magnetic microrobot and predicted that spiked ends geometry would result in better overall performance. Using the model as a design aid would help save time and reduce costs on the microrobot iteration and fabrication process. Despite manufacturing errors and limitations in the fabrication of more complex geometries, we show that the simulation model successfully can reproduce the effects of these errors for further predictions. Future developments may include accommodations for soft, elastomeric robot bodies without necessitating a rigid body assumption and additional modeling for wet environments.

Acknowledgment

The authors would like to acknowledge Seunghwan Jo and Prof. Martin Byung-Guk Jun for their assistance with laser cutting and access to their lab resources at Purdue University. The authors would also like to acknowledge the facility access at Birck Nanotechnology Center (Purdue University) and Georges Adam for his assistance with microrobot fabrication.

Conflict of Interest

There are no conflicts of interest.

Data Availability Statement

The authors attest that all data for this study are included in the paper. Data provided by a third party listed in Acknowledgment.

References

[1] Erkoc, P., Yasa, I. C., Ceylan, H., Yasa, O., Alapan, Y., and Sitti, M., 2018, "Mobile Microrobots for Active Therapeutic Delivery," Adv. Therapeutics, **2**(1), p. 1800064.

[2] Jiang, G.-L., Guu, Y.-H., Lu, C.-N., Li, P.-K., Shen, H.-M., Lee, L.-S., Yeh, J. A., and Hou, M. T.-K., 2010, "Development of Rolling Magnetic Microrobots," J. Micromech. Microeng., **20**(8), p. 085042.

[3] Hou, M. T., Shen, H. -M., Jiang, G. -L., Lu, C. -N., Hsu, I. -J., and Yeh, J. A., 2010, "A Rolling Locomotion Method for Untethered Magnetic Microrobots," Appl. Phys. Lett., **96**(2), p. 024102.

[4] Jing, W., Pagano, N., and Cappelleri, D. J., 2013, "A Tumbling Magnetic Microrobot with Flexible Operating Modes," Proceedings of IEEE International Conference on Robotics and Automation (ICRA), Karlsruhe, Germany, May 6–10, pp. 5514–5519.

[5] Jing, W., Pagano, N., and Cappelleri, D. J., 2013, "A Novel Micro-Scale Magnetic Tumbling Microrobot," J. Micro-Bio Rob., **8**(1), pp. 1–12.

[6] Tung, H.-W., Peyer, K. E., Sargent, D. F., and Nelson, B. J., 2013, "Noncontact Manipulation Using a Transversely Magnetized Rolling Robot," Appl. Phys. Lett., **103**(11), p. 114101.
[7] Pieters, R. S., Tung, H. -W., Sargent, D. F., and Nelson, B. J., 2014, "Non-Contact Manipulation for Automated Protein Crystal Harvesting Using a Rolling Microrobot," 19th IFAC World Congress, IFAC Proceedings Volumes, Cape Town, South Africa, Aug. 24–29, Vol. 47, Elsevier, Paper No. 3, pp. 7480–7485.
[8] Bi, C., Guix, M., Johnson, B. V., Jing, W., and Cappelleri, D. J., 2018, "Design of Microscale Magnetic Tumbling Robots for Locomotion in Multiple Environments and Complex Terrains," Micromachines, **9**(2), pp. 1–17.
[9] Bi, C., Niedert, E. E., Adam, G., Lambert, E., Solorio, L., Goergen, C. J., and Cappelleri, D. J., 2019, "Tumbling Magnetic Microrobots for Biomedical Applications," Proceedings of International Conference on Manipulation Automation and Robotics at Small Scales (MARSS), Helsinki, Finland, July 1–5, pp. 1–6.
[10] Mair, L., Chowdhury, S., Paredes-Juarez, G., Guix, M., Bi, C., Johnson, B., English, B., Jafari, S., Baker-McKee, J., Watson-Daniels, J. et al., 2019, "Magnetically Aligned Nanorods in Alginate Capsules (Maniacs): Soft Matter Tumbling Robots for Manipulation and Drug Delivery," Micromachines, **10**(4), p. 230.
[11] Niedert, E. E., Bi, C., Adam, G., Lambert, E., Solorio, L., Goergen, C. J., and Cappelleri, D. J., 2020, "A Tumbling Magnetic Microrobot System for Biomedical Applications," Micromachines, **11**(9), p. 861.
[12] Pawashe, C., Floyd, S., and Sitti, M., 2008, "Dynamic Modeling of Stick Slip Motion in An Untethered Magnetic Microrobot," Proceedings of Robotics: Science and Systems (RSS), Zurich, Switzerland, June 25–28, pp. 286–293.
[13] Pawashe, C., Floyd, S., and Sitti, M., 2009, "Modeling and Experimental Characterization of An Untethered Magnetic Micro-Robot," Int. J. Rob. Res., **28**(8), pp. 1077–1094.
[14] Xie, J., and Chakraborty, N., 2016, "Rigid Body Dynamic Simulation with Line and Surface Contact," Proceedings of IEEE International Conference on Simulation, Modeling, and Programming for Autonomous Robots (SIMPAR), San Fransisco, CA, Dec. 13–16, IEEE, pp. 9–15.
[15] Xie, J., and Chakraborty, N., 2018, "Rigid Body Dynamic Simulation with Multiple Convex Contact Patches," Proceedings of ASME International Design Engineering Technical Conferences and Computers and Information in Engineering Conference (IDETC/MSNDC), Quebec City, Canada, Aug. 26–29, Vol. 51838, ASME, p. V006T09A002.
[16] Xie, J., and Chakraborty, N., 2019, "Rigid Body Motion Prediction with Planar Non-convex Contact Patch," Proceedings of IEEE International Conference on Robotics and Automation (ICRA), Montreal, Canada, May 20–24, IEEE, pp. 7646–7652.
[17] Xie, J., Bi, C., Cappelleri, D. J., and Chakraborty, N., 2019, "Towards Dynamic Simulation Guided Optimal Design of Tumbling Microrobots," Proceedings of ASME International Design Engineering Technical Conferences and Computers and Information in Engineering Conference (IDETC/MR), Anaheim, CA, Aug. 18–21, Vol. 59230, ASME, p. V05AT07A057.
[18] Hu, W., Lum, G. Z., Mastrangeli, M., and Sitti, M., 2018, "Small-scale Soft-bodied Robot with Multimodal Locomotion," Nature, **554**(7690), pp. 81–85.
[19] Morozov, K. I., Mirzae, Y., Kenneth, O., and Leshansky, A. M., 2017, "Dynamics of Arbitrary Shaped Propellers Driven by a Rotating Magnetic Field," Phys. Rev. Fluids, **2**(4), pp. 1–29.
[20] Facchinei, F., and Pang, J.-S., 2007, *Finite-Dimensional Variational Inequalities and Complementarity Problems*, Springer Science & Business Media, Berlin/Heidelberg, Germany.
[21] Lotstedt, P., 1982, "Mechanical Systems of Rigid Bodies Subject to Unilateral Constraints," SIAM J. Appl. Math., **42**(2), pp. 281–296.
[22] Moreau, J. J., 1988, "Unilateral Contact and Dry Friction in Finite Freedom Dynamics," *Nonsmooth Mechanics and Applications*, P. D. Moreau, and J. J. Panagiotopoulos, eds., Springer, Berlin, Germany, pp. 1–82.
[23] Anitescu, M., Cremer, J. F., and Potra, F. A., 1996, "Formulating 3D Contact Dynamics Problems," Mech. Struct. Mach., **24**(4), pp. 405–437.
[24] Pang, J.-S., and Trinkle, J. C., 1996, "Complementarity Formulations and Existence of Solutions of Dynamic Multi-Rigid-Body Contact Problems With Coulomb Friction," Math. Program., **73**(2), pp. 199–226.
[25] Stewart, D. E., and Trinkle, J. C., 1996, "An Implicit Time-Stepping Scheme for Rigid Body Dynamics With Inelastic Collisions and Coulomb Friction," Int. J. Numer. Methods Eng., **39**(15), pp. 2673–2691.
[26] Pfeiffer, F., and Glocker, C., 2008, *Multibody Dynamics with Unilateral Contacts*, Wiley Inc., Hoboken, NJ.
[27] Acary, V., and Brogliato, B., 2008, *Numerical Methods for Nonsmooth Dynamical Systems: Applications in Mechanics and Electronics*, Springer Science & Business Media, Berlin/Heidelberg, Germany.
[28] Drumwright, E., and Shell, D. A., 2012, "Extensive Analysis of Linear Complementarity Problem (lcp) Solver Performance on Randomly Generated Rigid Body Contact Problems," Proceedings of IEEE/RSJ International Conference on Intelligent Robots and Systems (IROS), Vilamoura, Algarve, Portugal, Oct. 7–12, IEEE, pp. 5034–5039.
[29] Todorov, E., 2014, "Convex and Analytically-invertible Dynamics with Contacts and Constraints: Theory and Implementation in Mujoco," Proceedings of IEEE International Conference on Robotics and Automation (ICRA), Hong Kong, China, Aug. 18–21, IEEE, pp. 6054–6061.
[30] Anitescu, M., and Potra, F. A., 1997, "Formulating Dynamic Multi-rigid-body Contact Problems with Friction As Solvable Linear Complementarity Problems," Nonlinear Dyn., **14**(3), pp. 231–247.
[31] Anitescu, M., and Potra, F. A., 2002, "A Time-stepping Method for Stiff Multibody Dynamics with Contact and Friction," Int. J. Numer. Methods Eng., **55**(7), pp. 753–784.
[32] Tzitzouris, J. E., 2001, "Numerical Resolution of Frictional Multi-Rigid-Body Systems Via Fully Implicit Time-Stepping and Nonlinear Complementarity," Ph.D. thesis, Johns Hopkins University, Baltimore, MD.
[33] Chakraborty, N., Berard, S., Akella, S., and Trinkle, J. C., 2014, "A Geometrically Implicit Time-Stepping Method for Multibody Systems With Intermittent Contact," Int. J. Rob. Res., **33**(3), pp. 426–445.
[34] Erdmann, M., 1994, "On a Representation of Friction in Configuration Space," Int. J. Rob. Res., **13**(3), pp. 240–271.
[35] Goyal, S., Ruina, A., and Papadopoulos, J., 1991, "Planar Sliding With Dry Friction Part 1. Limit Surface and Moment Function," Wear, **143**(2), pp. 307–330.
[36] Howe, R. D., and Cutkosky, M. R., 1996, "Practical Force-Motion Models for Sliding Manipulation," Int. J. Rob. Res., **15**(6), pp. 557–572.
[37] Murray, R. M., Li, Z., and Sastry, S. S., 1994, *An Mathematical Introduction to Robotic Manipulation*, CRC Press, Boca Raton, FL.
[38] Fearing, R. S., 1995, "Survey of Sticking Effects for Micro Parts Handling," Proceedings of IEEE/RSJ International Conference on Intelligent Robots and Systems. Human Robot Interaction and Cooperative Robots, Pittsburgh, PA, Aug. 5–9, Vol. 2, IEEE, pp. 212–217.
[39] Diller, E., 2011, "Micro-Scale Mobile Robotics," Foundat. Trends Rob., **2**(3), pp. 143–259.
[40] Arscott, S., 2014, "Su-8 As a Material for Lab-on-a-Chip-Based Mass Spectrometry," Lab. Chip., **14**(19), pp. 3668–3689.
[41] Nemani, K. V., Moodie, K. L., Brennick, J. B., Su, A., and Gimi, B., 2013, "In Vitro and in Vivo Evaluation of Su-8 Biocompatibility," Mater. Sci. Eng.: C, **33**(7), pp. 4453–4459.
[42] Raj M, K., and Chakraborty, S., 2020, "PDMS Microfluidics: A Mini Review," J. Appl. Polym. Sci., **137**(27), p. 48958.
[43] Goyal, S., Ruina, A., and Papadopoulos, J., 1991, "Planar Sliding With Dry Friction Part 1. Limit Surface and Moment Function," Wear, **143**(2), pp. 307–330.
[44] Howe, R. D., and Cutkosky, M. R., 1996, "Practical Force-Motion Models for Sliding Manipulation," Int. J. Rob. Res., **15**(6), pp. 557–572.
[45] Trinkle, J. C., Pang, J. -S., Sudarsky, S., and Lo, G., 1997, "On Dynamic Multi-Rigid-Body Contact Problems With Coulomb Friction," ZAMM-J. Appl. Math. Mech., **77**(4), pp. 267–279.
[46] Trinkle, J. C., Tzitzouris, J., and Pang, J. -S., 2001, "Dynamic Multi-Rigid-Body Systems With Concurrent Distributed Contacts," Philos. Trans. R. Soc. London A: Math., Phys. Eng. Sci., **359**(1789), pp. 2575–2593.
[47] Akin, S., Gabor, T., Jo, S., Joe, H., Tsai, J.-T., Park, Y., Lee, C. H., Park, M. S., and Jun, M. B.-G., 2020, "Dual Regime Spray Deposition Based Laser Direct Writing of Metal Patterns on Polymer Substrates," ASME J. Micro Nano-Manuf., **8**(2), p. 024511.